國立交通大學

材料科學與工程學系

博 士 論 文

氟化非晶質碳膜之性質

The Properties of Fluorinated Amorphous Carbon Films

研　究　生：黃昆平

指導教授：林　鵬　教授

中 華 民 國 九十三 年 六 月

氟化非晶質碳膜之性質
The Properties of Fluorinated Amorphous Carbon Films

研 究 生：黃昆平　　Student：Kun-Ping Huang

指導教授：林　鵬　　Advisor：Pang Lin

國 立 交 通 大 學

材 料 科 學 與 工 程 學 系

博 士 論 文

A Thesis

Submitted to Department of Materials Science and Engineering

College of Engineering

National Chiao Tung University

in partial Fulfillment of the Requirements

for the Degree of

Doctor of Philosophy

in

Materials Science and Engineering

June 2004

Hsinchu, Taiwan, Republic of China

中華民國九十三年六月

氟化非晶質碳膜之性質

學生：黃昆平　　　　　　　　　　　　　　　　　指導教授：林　鵬

國立交通大學材料科學與工程學系博士班

摘　　　要

本研究是用四氟化碳(CF_4)及乙炔(C_2H_2)為前驅物，以射頻輔助電子迴旋共振化學氣相蒸鍍法來沉鍍非晶質氟化碳(a-C:F)膜。鍍膜時所使用的氣體流量比 R 從 0.90 至 0.98，其中 $R = CF_4/(CF_4+C_2H_2)$；而成膜後的退火是在 300℃純氮氣氣氛下進行。霍氏紅外線光譜儀(FTIR)及 X 光光電子光譜儀(XPS)被用來鑑定非晶質氟化碳膜的化學健結及氟含量；而高解析電子能量損失光譜儀(HREELS)被用來檢測電子的結構。較高的四氟化碳氣體流量比會產生較多的線性 sp^3 結構，因而使得非晶質氟化碳膜更平滑及更柔軟。

本研究製作出 R = 0.98 成膜及退火後介電常數能達 1.5 及介電強度超過 35 MV/cm 的非晶質氟化碳膜。而奈米孔(nanovoid)及 sp^2/sp^3 鍵結比例可被用來討論及闡述關於電性量測時觀察到膜的巨大電流跳躍及電傳導現象。

成膜及退火過後的氟化非晶質碳膜的光學性質與類鑽石膜 (a-C:H)性質相仿，其中 R = 0.98 非晶質氟化碳膜擁有較類鑽石膜(0.07 奈秒)長的 0.34 微秒的螢光壽命及較類鑽石膜(~2.5 eV)寬的 2.75 eV 的光能隙。同時，非晶質氟化碳膜的短載子壽命會使得螢光光譜產生藍偏的現象，此現象與非晶質矽(a-Si:H)的性質相似。

退火會改變非晶質氟化碳膜的結構及組成，非晶質氟化碳膜的機械及物理性質是隨著氟化碳的鍵結及電子結構的改變而變化。sp^3 鍵結的含

量隨著氟化非晶質碳膜的氣體流量比（ R)氟含量增加而增加，sp^3鍵結的增加會使得膜的漏電流減小、介電常數下降、能帶變寬………等等，然而這些 sp^3鍵結經鑑定結果絕大份是以練狀型態出現，故會使得氟化非晶質碳膜質地更平滑而且柔軟。此外，氟化非晶質膜氟含量的增加則有助於懸空鍵結(dangling bond)密度的降低。

The Properties of Fluorinated Amorphous Carbon Films

student：Kun-Ping Huang Advisors：Dr. Pang Lin

Department of Materials Science and Engineering
National Chiao Tung University

ABSTRAC

Fluorinated amorphous carbon (a-C:F) films were deposited by RF bias assisted microwave plasma electron cyclotron resonance chemical vapor deposition (ECR-CVD), using tetrafluoromethane (CF_4) and acetylene (C_2H_2) as precursors. The deposition process was performed at flow ratios from R = 0.90 to R = 0.98, where R = CF_4/(CF_4+C_2H_2). The samples were annealed at 300℃ for 30 min. in a N_2 atmosphere. Both Fourier transform infrared absorption spectrophotometer (FTIR) and X-ray photoelectron spectroscopy (XPS) were used to observe the a-C:F film chemical bond and fluorine concentration respectively, and a high resolution electron energy loss spectrometer (HREELS) was applied to detect the electronic structure. The higher CF_4 flow ratio generated more sp^3 linear structures, and it made the a-C:F film smoother and softer.

A low dielectric constant of around 1.5 and high dielectric strength beyond 35 MV/cm were obtained in the as-deposited and after annealing

conditions, respectively. The huge current surge and electrical conductivity of the films were discussed on the basis of the nano-voids and sp^2/sp^3 bonding fractions as derived from the above observations.

The optical properties of a-C:F films are similar to those of a-C:H films. The 0.34 μsec photoluminescence lifetime of R = 0.98 a-C:F film is longer than that of diamond-like carbon films. The ~ 2.75 eV optical band gap of the R = 0.98 a-C:F film is wider than diamond-like carbon films. The short carrier lifetime in the a-C:F film made the PL peak blue-shift. Such condition is similar to a-Si:H films.

The annealing changed both the structure and composition of the a-C:F film. The type of fluorocarbon bond and electronic structure characterized the a-C:F film mechanical and physical properties. The density of sp^3 bonds is positively proportional to the gas flow ratio in ECR-CVD and fluorinate concentration of a-C:F films. The increase of sp^3 bonds lowers the leakage current as well as the dielectric constant of the a-C:F films. At the same time the increase of sp^3 bonds helps to generate the optical band gap. However, as most of the sp^3 bonds are consisted in chain structure, they make the a-C:F films smoother and softer. The sp^3 bonds help to decrease the density of the dangling bonds in a-C:F films.

誌　　謝

博士班的生涯裏，首先要感謝我的指導教授--林鵬，施漢章(清大)及 Dr. S. Roth(司徒加特—馬克思普朗克研究所)教授在研究期間的各項指導。感謝曾俊元及謝宗雍老師於口試時的各項指教。感謝李正中、朱聰明、郭行健及蔡增光學長在實驗上的指導；蔡尚華、劉元文、邱紹裕、方照詒、王怡凱、溫子稷及同學在學業上的切磋；交大電子陶瓷實驗室的陳重安、蔡明典、黃加星、陳光中、盧俊安、李思毅、蘇愷農、賴柏文、李仁豪、謝文斌、林志豪、黃雅君、范瑋寒、劉奎府及陳良湘……等學弟妹在各項實驗上的協助，清大微波電漿氣鍍室的賴識翔、鐘武均、陳雁鈴及潘易民……等學弟妹於各項實驗上的幫助。特別感謝張德富及邱博文學弟在 HRTEM 及電性量測上的協助。此外感謝交大田徑隊所有一起練過的隊員讓我在交大校園生活多采多姿；司徒加特華僑分會曹增東會長，晏水平、蔣昱、廖海濤、Martti Kaempgen 和 Mirko Sonntag……等等豐富了我在德國司徒加特大學的留學生涯，國科會駐德國辦事處所有同仁在留德期間生活上無為不至的照顧。最後，感謝我最親愛家人的全力支持，讓我平安順利讀完交大博士班。

Contents

Abstract (in Chinese)……………………………….........i

Abstract (in English)……………………………………iii

Acknowledgment (in Chinese)………………………...v

Contents……………………………………………….vi

Tables Caption……………………..……………........xi

Figures Caption………………………………………..xii

Chapter 1 Overview……………………………………1~17

1-1 General Background………………………….......1

1-2 Polarization……………………………………......5

1-2-1 Electrostatic Equation with Dielectrics……….…….……..5

1-2-2 Mechanisms of Polarization………………………………..7

1-3 Plasma-Chemical Vapor Deposition………..….......11

1-3-1 High Density Plasma Source…………………………...11

1-3-2 Electron Cyclotron Resonance CVD……………….….13

Reference……………………………………………....16

Chapter 2 Literature Review……………………......18~29

2-1 Low Dielectric Constant Materials………….........18

2-2 Fluorinated Amorphous Carbon…………….........24

1896

Reference……………………………………………….......27

Chapter 3 Characterization Techniques for Amorphous Carbons Films…………………….…...30~35

3-1Introduction………………………………………….....30

3-2 Analyses and Measurements Techniques…………….....31

3-2-1 Optical Emission Spectroscope (OES)…………………....31
3-2-2 Thermal Desorption Analyze (TDA)……………………...31
3-2-3 Atomic Force Microscope (AFM)……………………......31
3-2-4 Nano-indentor…………………………………………..32
3-2-5 Field-Emission Scanning Electron Microscope (FESEM)………………………………………………32
3-2-6 Glow Discharge Spectrometer (GDS)…………………....32
3-2-7 Fourier-Transform Infrared Spectrometer (FTIR)……..…33
3-2-8 X-ray Photoelectron Spectroscope (XPS)………………...33
3-2-9 High-Resolution Transmission Electron Microscope (HRTEM)…………………………………………...……34
3-2-10 High-Resolution Electron Energy Loss Spectroscope (HREELS)…………………………………………….....34
3-2-11 Electron Paramagnetic resonance (EPR)………………...34
3-2-12 Capacitance-Voltage (C-V) Curve……………………......34
3-2-13 Current-Voltage (I-V) Curve…………………………..35
3-2-14 n&k Analyzer…………………………………………….35
3-2-15 UV-Visible Spectrophotometer (UV/VI)……………......35
3-2-16 Photoluminescence (PL)……………………………......35
3-2-17 Pulse Laser……………………………………………......35

Chapter 4 Synthesis of a-C:F Film…………………36~41

4-1 Introduction…………………………………………36

4-2 Experiment……………………………………………...….36

4-3 Sample Preparation…………………………………38

4-3-1 Substrate Cleaning……………………………………...38
4-3-2 Low k Film Deposition………………………………....38
4-3-3 Annealing………………………………………………....39

4-4 Physical Analysis……………………………………...40

4-5 Chemical Analysis…………………………………....40

Reference……...………………………………………...41

Chapter 5 Physical Properties…...….…..……………...42~51

4-1 Introduction……………………………………........42

4-2 Results and Discussion…………………………......42

4-3 Summary…………………………………………….....50

Reference……………………………………………..…....51

Chapter 6 Chemical Properties...............................52~74

6-1 Introduction……………………………………..……52

6-3 Results and Discussion…………………………..…53

6-4 Summary……………………………………...…..…71

Reference……………………………………………..…...72

Chapter 7 Electric Properties……………………..…..75~84
7-1 Introduction…………………………………..……75
7-2 Experiment……………………………………..…..75
7-2-1 Insulator deposition…………………………….....…77
7-2-2 Metal Thin Film Deposition……………………………77
7-3 Results and Discussion…………………………......77
7-4 Summary……………………………………..….83
Reference……………………………………..…...83

Chapter 8 Optical Properties……………………..…....85~93
8-1 Introduction……………………………………..…..85
8-2 Experiment……………………………………….....85
8-3 Results and Discussion…………………………......87
8-4 Summary……………………………………..…..92
Reference……………………………….…………….....92

Chapter 9 Conclusions and Suggestion for Future Work……………………………………..94~95
9-1 Conclusions………………………………………………94
9-2 Suggestion for Future Work………………..………...95

Resume (in Chinese)……………………………………...…96

Publication List………………………………………………98

Tables Caption

Table 2-1. Low dielectric constant materials for ULSI interconnects........22

Table 2-2. Basic requirements for low dielectric constant materials…......23

Table 5-1. Primary electron collisions……………………..……………..44

Table 5-2. The hardness of a-C:F films at as-deposited and after annealed……………………………………………………….49

Table 6-1. Summary of FT-IR absorption peaks…………………………56

Table 6-2. ESCA chemical composition (at. %) of the a-C:F films as-deposited and after being annealed at 300°C……………....62

Figures Caption

Figure 1-1 The architecture of multilevel interconnect metallization……4

Figure 1-2 Decrease in interconnect delay and improved performance are achieved using copper and low-k dielectrics…….………4

Figure 1-3 The cross-section of interconnect system with parasitic capacitance…………………………………………..……5

Figure 1-4 shows the schema of polarization mechanism………………10

Figure 1-5 Frequency dependence of real part of the dielectric function…………………………………………………...10

Figure 1-6 shows high-density sources. They are (a) ECR source (b) Helicon source (c) Helical resonator and (d) Inductive source……..…………………………………………………13

Figure 1-7 The schematic illustration of the ECR microwave plasma CVD system……………………………………………..14

Figure 1-8 A charged particle is forces by magnetic field to move along a spiral path. ECR with reinforced plasma is obtained, if the spiral movement and the microwave field are synthesized....15

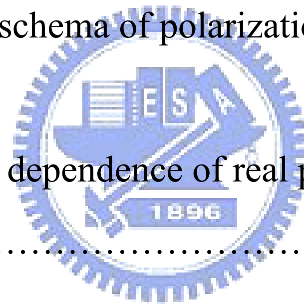

Figure 2-1 Summary timeline of the materials anticipated in future generation multilevel interconnect structures………..……...19

Figure 4-1 shows the measurement methods of chemical and physical Properties………………………………………….…………...37

Figure 4-2 shows the illustration of the ECR microwave plasma CVD system…………………………………………..…….39

Figure 5-1 Optical emission spectra obtained in C_2H_2 and CF_4 mixed gas discharge at 600W source power -200V rf bias, and 20 m Torr in the ECR-CVD……………………….……………....45

Figure 5-2 Comparisons of the plasma optical emission spectra for R = 0.97 and R = 0.90…………………………………….…..…45

Figure 5-3 shows the deposition rate of a-C:F films……………………47

Figure 5-4. The Film's thickness change after annealing as a function of flow ratio R………………………………….....................47

Figure 5-5 shows the TDA result of R = 0.90 a-C:F film. 31, 50 and 69 mean the molecule weight of CF, CF_2 and CF_3……………......48

Figure 5-6 shows the AFM images of R = 0.90 a-C:F films. (a) is

as-deposited, and (b) is after annealed……………….……….....49

Figure 5-7 shows the hardness of a-C:F films at as-deposited and after annealing………..…………………………….……….....50

Figure 6-1 Comparing the FTIR spectrums of as-deposited a-C:F films…………………………………………………………..55

Figure 6-2 FTIR spectroscopy of the a-C:F film, (a) as-deposited at R = 0.97, (b)after being annealed at R = 0.97, (c) as-deposited at R = 0.90, (d) after being annealed at R = 0.90………… ..55

Figure 6-3 Deconvoluted C 1s spectrum of a-C:F film at R = 0.97 as-deposited obtained by XPS analysis…………….………...58

Figure 6-4 Fluorine concentration in the film as functions of flow ratio R…..……………………………………………………….59

Figure 6-5 C(1s) spectra change of the as-deposited a-C:F films as functions of the flow ratio R. The integrated intensities of the C(1s) spectra are normalized………………………………..60

Figure 6-6 Deconvolution result of the a-C:F film C 1s spectrum for R = 0.97 and R = 0.90 at as-deposited and after being annealed obtained by ESCA analysis…………………………….…...62

Figure 6-7 Comparisons of the HREELS spectra in the carbon K-edge region……………………………………………………..64

Figure 6-8 Carbon K-ionization edge spectra obtained from R = 0.97 as-deposited. The fit obtained when using three Gaussian peaks centered at 285, 287, and 293 eV…………………….67

Figure 6-9 shows the sp^3% of as-deposited and after annealing a-C:F films……………………………………………….……...67

Figure 6-10 (a) is the R = 0.98 as-deposited HRTEM image, and (b) is after annealed one………………………………..………...69

Figure 6-11 (a) is the HRTEM image of R = 0.95 a-C:F film after annealing , and (b) is the HREELS image by carbon element mapping of same film…………………………………………………….69

Figure 6-12. Dangling bond density of the a-C:F films at R = 0.97 and R = 0.90 as deposited………………………..………......71

Figure 7-1 shows the schematic structure of MIM (Pt/a-C:F/Pt)……….76

Figure 7-2 shows the measurement methods of electronic properties…..76

Figure 7-3 Dielectric constant of the films as function of the CF_4 flow

ratio R……………………….…………………….…………………..78

Figure 7-4 Leakage current of the a-C:F films of (a) R = 0.98, (b) R = 0.97, (c) R = 0.95, (d) R = 0.90……………………………80

Figure 7-5 Electrical conductivity of the annealed films as a function of the CF_4 flow ratio R……………………………………….....82

Figure 7-6 sp^2 bonding fraction of the annealed films as a function of the CF_4 flow ratio R…………………………………….…...82

Figure 8-1 The Experiment flowchart for optical measurement………..86

Figure 8-2 PL spectra produced at R=0.97 and at R=0.90 of a-C:F films for both as-deposited and after-annealed at 300°C…….........88

Figure 8-3 shows the photoluminescence lifetime of as-deposited and 300℃ annealing a-C:F films…………………………........89

Figure 8-4 UV/VI spectra of both R=0.97 and 0.90 of the a-C:F films as-deposited and after-annealed at 300°C……………..91

Figure 8-5 shows the energy gap of as-deposited and 300℃ annealing a-C:F films……………………………………………….…….91

Chapter 1

Overview

Dielectric and optical materials have been playing an important role in the evolution of today's electrical engineering, electronics, and information technology. The materials involved are typically crystalline, amorphous oxides, organic compounds and polymers. They are employed as bulk materials and, most often, as thin films.

Dielectrics are used as insulating materials due to their property of polarization to modify the dielectric function of the vacuum, e.g. enhancing the capacity (i.e. the ability to store charges) of capacitors. They do not conduct electricity due to the very low density of free charge carriers. Here, the electrons are bound to microscopic regions within the material, i.e. the atoms, molecules, or clusters, instead of being freely movable in and out of a macroscopic system.

1-3 General Background

In the past 40 years, the electronics industry owes its phenomenal growth to the development of faster, cheaper, lighter, and smaller semiconductor products. So far the minimum scaling size has reached the maximum of transistor density. It is recognized, however, that device physics is not the first limiting factor to the continued performance improvement for systems. The challenge will be how to carry electric power and how to distribute the clock signals that control the timing and synchronize the operation. The challenge extends beyond the materials

properties, technologies and as well as the system architecture. On the other hand, the semiconductor industry is in progress. It accelerates the progress of Moore's law.

The dimensional scaling of back-ended interconnection (Fig. 1-1) results in the fact that not only the line-width and spaces between metal interconnections are decreased, but also the length of the interconnection lines will increase. This process will increase the RC time delay due to the higher wire resistance (R) of the narrower metal leads and the higher intra/inter-level capacitance (C) between the tightly spaced interconnections. While the interconnecting circuits in the cross-sectional area are reduced, the density of conducting current will rise and cause electromigration to be worse[1]. Furthermore, the length of the interconnected lines will increase, owing to the larger chip size and the multilevel metallization, required for increased functional complexity and packing density of the integrated circuits. As a result, it is the characteristics of the interconnections that dominate the total circuit propagation (RC) delay, not the scaling of the active devices (Fig. 1-2)[2].

According to Fig. 1-3, we assume that the minimum metal pitch is equal to the twice of the metal width plus the dielectric thickness. This assumption is the same for the metal lines in between. Therefore, we consider the first-order approximation of the time delay τ and the power consumption P as follows.

$$\tau = RC = 2\rho\varepsilon\left(\frac{L_m^2}{W^2} + \frac{L_m^2}{t_m^2}\right) \qquad (1)$$

$$p = \alpha C f V^2 \qquad (2)$$

, with

$$R = \rho \frac{L_m}{W t_m} \tag{3}$$

$$C = C_{output} + C_{wire} + C_{input}$$

$$\approx (C_L + C_V) = 2\varepsilon \left(\frac{L_m t_m}{W} + \frac{L_m W}{t_m} \right) \tag{4}$$

where ρ and ε are the resistivity and the permittivity, respectively. L_m, W and t_m are the length of interconnected line, and thickness of the metal, respectively. α, f and V are the wire activity (i.e., when the wire is transferring a signal), frequency, and applied voltage. According to these equations, factors affecting the RC time delay can be divided into two groups: the material property (ρ and ε) and the geometric structure (L_m, W and t_m). Since it is not easy to reduce the time constant by changing the geometric structure, such as the height and pitch of wire, there are two approaches to minimize the resistance × capacitance (RC) delay. One is to reduce the resistivity of the RC delay by using copper as the conductor for multi-interconnections. Copper has resistivity of 1.694 μΩ-cm which is much lower than the 2.69 μΩ-cm of aluminum. The other is to reduce the coupling capacitance between the metal lines. This method requires low dielectric constant (low k) materials, which can lower line to line capacitance to reduce the signal propagation delay, minimize cross-talk noise in interconnections, and alleviate power dissipation issue[3, 4].

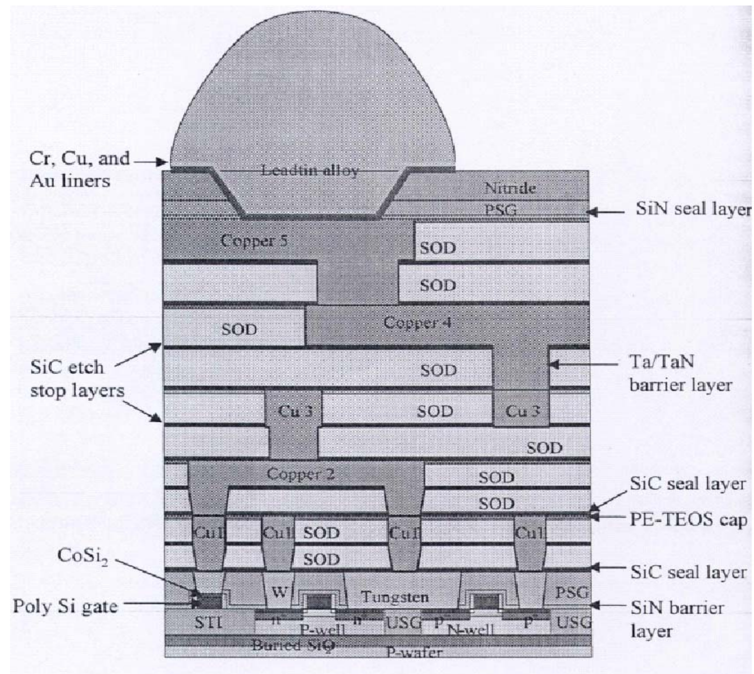

Figure 1-1. The architecture of multi-level interconnected metallization.

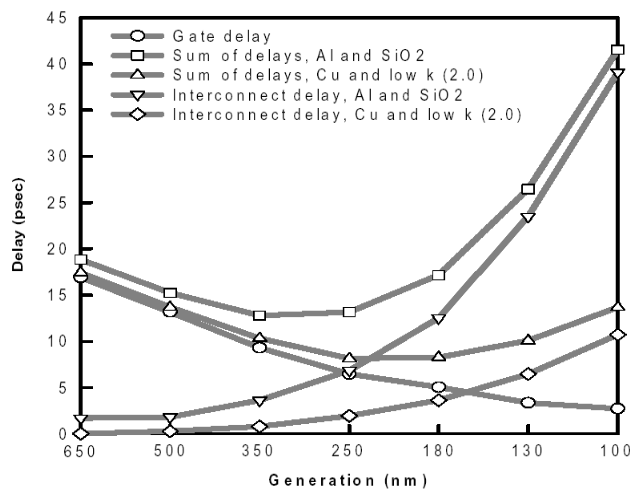

Figure 1-2. Decrease in interconnected delay and improved performance are achieved by using copper and low-k dielectrics. (Source: Semiconductor International 2001)

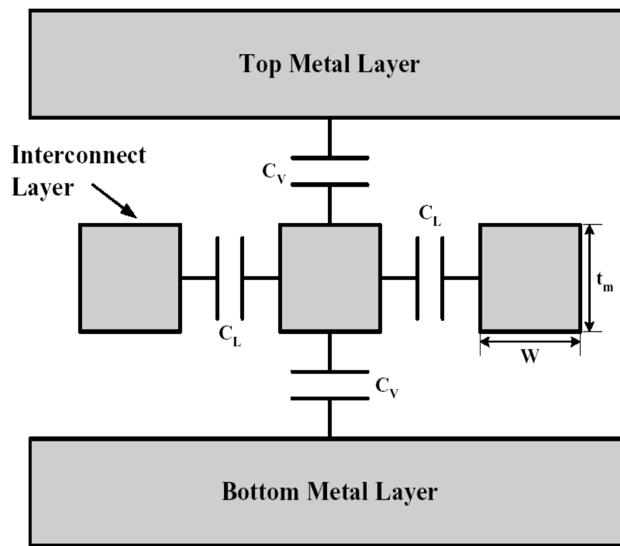

Figure 1-3. The cross-section of interconnected system with parasitic capacitance.

1-2 Polarization

Polarization is the separation of positive and negative charge barycentres of bound charges. If this separation is induced by an applied electric field, it is called dielectric polarization. Such property of the material -- measurement of its own polarization ability -- is called the dielectric constant (or: permittivity) ε_r. There are several mechanisms for the dielectric polarization determined by the polarizable unit (atom, cation-anion pair, orientable permanent dipole, etc.).

1-2-1 Electrostatic Equation with Dielectrics

According to the Poisson equation, each free charge acts as a source

for the dielectric displacement D:

$$divD = \rho_{free} \tag{5}$$

where ρ_{free} denotes the density of free (conduction) charges. Based on this relation, the overall charge neutrality of matter in an external field is described by:

$$D = \varepsilon_0 E + P \tag{6}$$

The term $\varepsilon_0 E$ describes the vacuum contribution to the displacement D caused by an externally applied electric field E, and P represents the electrical polarization of the matter in the system. This relation is independent of the cause of the polarization. The polarization may exist spontaneously (pyroelectric polarization), it may be generated by mechanical stress (piezoelectric polarization), or, induced by an external electric field (dielectric polarization).

In our case of a dielectric polarization, the polarization of the matter is related to the electric field by

$$P = \varepsilon_0 X_e E \tag{7}$$

Which leads to

$$D = \varepsilon_0 (1 + X_e) E = \varepsilon_0 \varepsilon_r E \tag{8}$$

X_e : electrical susceptibility

ε_r : relative permittivity (or: dielectric constant).

If χ_e or ε_r themselves are field-dependent, e.g. being reduced for high electric fields, tunable dielectrics are achieved.

1-2-2 Mechanisms of Polarization

In general, one can distinguish between four different types of polarization[5, 6]:

- *Electronic polarization* describes the displacement of the negatively charged electron shell against the positively charged nucleus. Since all matter is built from atoms, this is true for dielectrics in general. The electronic polarisability α_{el} is approximately proportional to the volume of the electron shell. Thus, large atoms have a large electronic polarisability. Since the atomic radius is temperature-independent, generally the temperature dependence of α_{el} can be neglected.
- *Ionic polarization* is observed in materials with ionic bonds (i.e. ionic crystals) and described as the mutual displacement of the positive and negative sublattices under the influence of an applied electric field. In general the temperature dependence of the ionic polarisability α_{ion} is weakly positive because of the thermal expansion of the lattice.
- *Orientation polarization* describes the alignment dipoles. In many substances there are molecules – either regular constituents or impurities – which carry a (permanent) electric dipole moment. If these dipoles are mobile or, at least able to reorient themselves by rotation, they do contribute to the dielectric polarization by the so-called orientation polarization. At ambient temperature, usually all dipole moments are mutually compensated because of the orientational disorder, i.e. the statistical distribution of their directions. An electric field, on the other hand, generates a preferred direction for the dipoles, while the thermal movement of the atoms perturbs the temperature. The solution is given by the so-called Langevin function[7]. For all

technically applied cases, the polarisability originating from permanent dipole moments **p** is given by

$$\alpha_{or} = \frac{p^2}{3k_B T} \tag{9}$$

where k_B denotes the Boltzmann constant and T the absolute temperature measured in Kevin.

The strong temperature dependence is one of the main characteristics of the orientation polarization.

- *Space charge polarization* describes a polarization effect in a dielectric material which shows spatial inhomogeneities of charge carrier densities. Space charge polarization effects are not only of importance in semiconductor field-effect devices[8], they also occur in ceramics with electrically conducting grains and insulating grain boundaries[9] as well as in composite material systems in which metallic particles are isolated in polymer or glass matrices.

Figure 1-4 shows the schema of these four kinds of polarization mechanism. The total polarizability (i.e. $\alpha_{total} = \alpha_e + \alpha_i + \alpha_o + \alpha_s$) of dielectric material results from the four contributions discussed above. The space charge only can happen in poly crystallize materials. For amorphous materials the total polarization is $\alpha_{total} = \alpha_e + \alpha_i + \alpha_o$. The polarization depends on the frequency of applied field. The polarizability of materials appears to decrease with increasing frequency. Each contribution stems from a short range movement of charges that respond to an electric field on

different time scales and, hence, through a Fourier transform, in different frequency regimes. The dispersion of the real part of the polarizability function is shown in Figure 1-5, converting the entire frequency spectrum. At optical frequencies (10^{14} Hz), only the lowest species, electrons, can contribute polarization in the materials. At lower frequency, ionic polarization of induced dipoles such as a carbonyl group can occur in the infrared (10^{12} Hz) or lower frequency regimes. Orientation polarization is the redistribution of charge when a group of atoms with a permanent dipole align in response to the electric field. In the solid state, alignment of permanent dipoles requires considerably more time than electronic or atomic polarization, occurring at microwave (10^{9} Hz) or lower frequencies[10]. The space charge polarization is caused by a drift of mobile ions or electrons which are confined to outer or inner interfaces. Depending on the local conductivity, the space charge polarization may occur over a wide frequency range from mHz up to MHz[6].

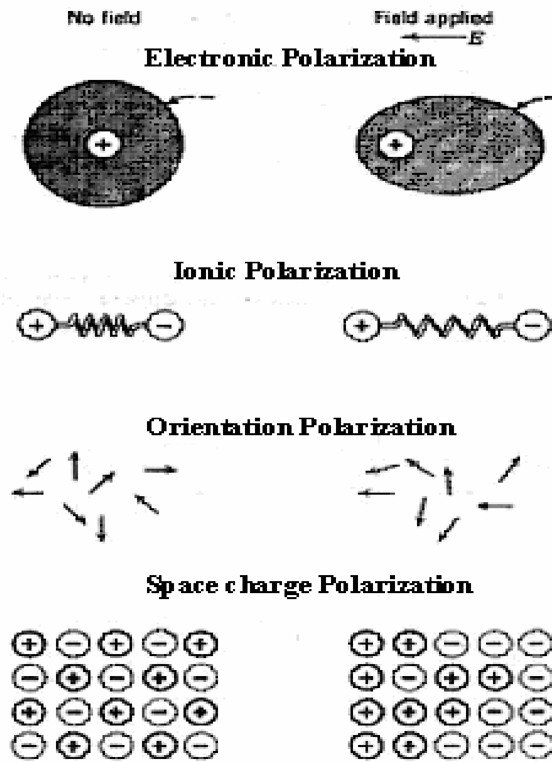

Figure 1-4 shows the schema of polarization mechanism.

1896

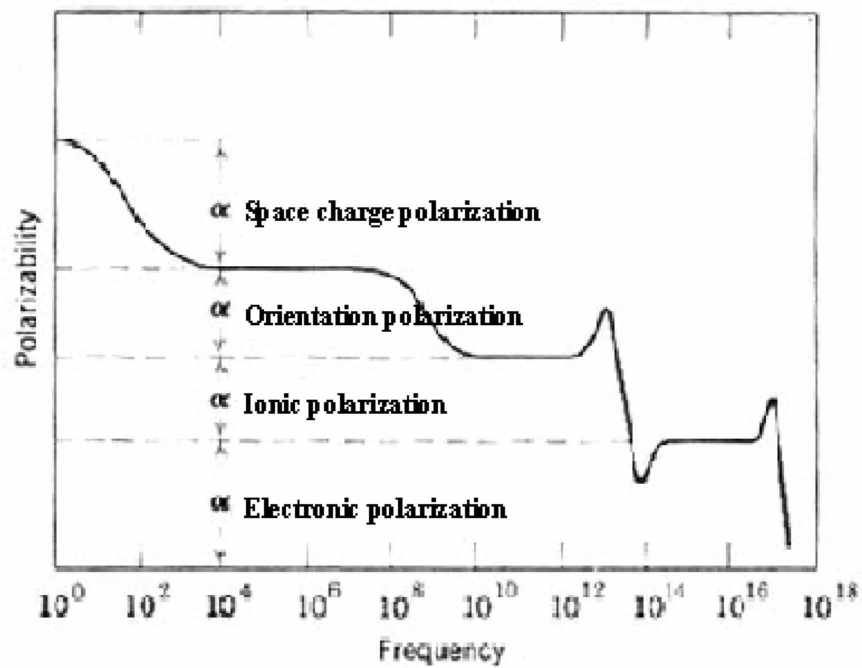

Figure 1-5 Frequency dependence of real part of the dielectric function.

1-3 Plasma-Chemical Vapor Deposition

At the end of World War II, chemical vapor deposition (CVD) expanded rapidly as researchers realized its advantages for the production of coatings and freestanding shapes. Unfortunately, with the introduction of polymer and low melting point metal films, the CVD was severely degraded by the presence of defects such as dislocations, stacking faults, vacancies, and interstitial species. These considerations often preclude the use of high (>300℃) temperatures during film formation. Furthermore, even if elevated temperatures can be tolerated, film morphology and phase structure often tied directly to deposition rate should be controlled separately. The above limitations can generally be circumvented if the energy necessary for bond cleavage is supplied by the high energy electrons in glow discharge or plasmas[11, 12].

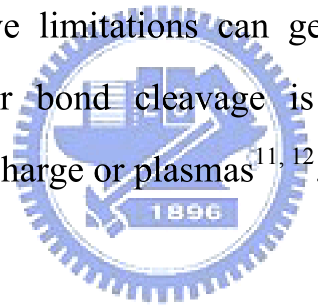

1-3-1 High Density Plasma Source

A few examples are shown schematically in Figure 1-6. They have the common features of power transfer across dielectric windows and separate bias supply at the wafer electrode. Figure 1-6 a is an electron cyclotron resonance (ECR) source. Electromagnet coils surrounding the cylindrical source chamber generate an axially varying dc magnetic field. Microwave power is injected axially through dielectric windows into the source plasma, where it excites a right-hand circularly polarized wave that propagates to a resonance zone, for cold electrons at $\omega = \omega_{ce}$, where the wave is absorbed. Here $\omega = 2\pi f$ is applied radian frequency and $\omega_{ce} = eB/m$

is the electron gyration frequency at resonance. For the typical microwave frequency used, f = 2450 MHz, the resonance magnetic field is B ≈ 875 G. The plasma streams out of the source into the process chamber in which the wafer is located.

A helicon source is shown in Fig. 1-6 b. A weak (50-200G) dc axial magnetic field together with an rf-driven antenna placed around the dielectric cylinder that forms the source chamber allows excitation of a helicon wave within the source plasma. For the helical resonator source is shown in Fig. 1-6 c, the external helix and conducting cylinder surrounding the dielectric discharge chamber form a slow wave structure, i.e., supporting an electromagnetic wave with phase velocity much less than the velocity of light. Efficient coupling of the rf power to the plasma is achieved by excitation of a resonant axial mode. An inductive (or transformer) coupled source is shown in Fig. 1-6 d. Here the plasma acts as a single-turn conductor that is coupled to a multi-turn non-resonant rf coil across the dielectric discharge chamber; rf power is inductively coupled to the plasma by transformer action. In contrast to ECR and helicon sources, a dc magnetic field is not required for efficient power coupling in helical resonator or inductive sources[13].

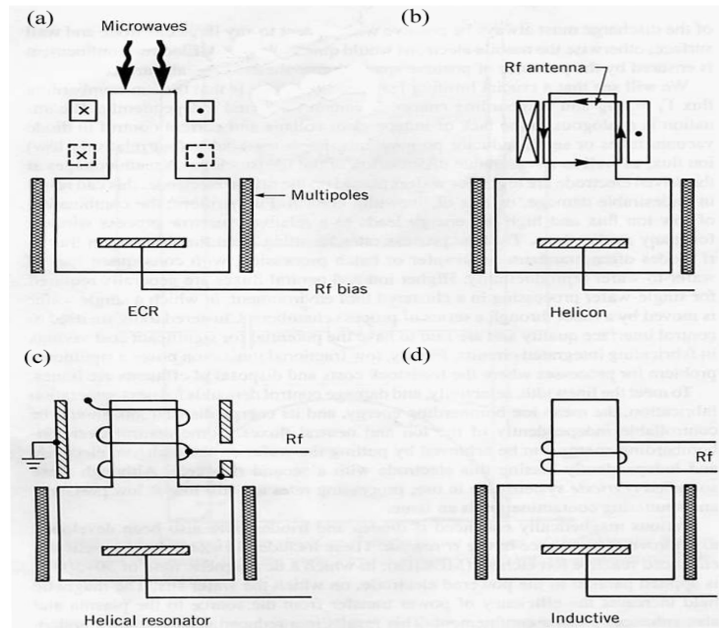

Figure 1-6 shows high-density sources. They are (a) ECR source (b) Helicon source (c) Helical resonator and (d) Inductive source.

1-3-2 Electron Cyclotron Resonance CVD

The electron cyclotron resonance (ECR) CVD system is a high density plasma system. It can be used as CVD or dry etching functions. The ECR CVD was used to synthesize the fluorinated amorphous carbon films in the paper. Microwave power 2,45 GHz frequency is supplied to a plasma chamber through a quartz entrance window and waveguide. The magnetic field of 875 Guass for the ECR plasma excitation is generated by the coils surrounding the resonance volume and is applied perpendicularly to the surface of the substrate. A radio frequency (RF) (13.56 MHz) bias is also applied to the substrate. In order to avoid the interaction of electromagnetic fields which are between microwave and RF. The aluminum grid was used

to separate the electromagnetic field (Figure 1-7). The plasma stream is introduced into the deposition chamber, which is pumped down to the base pressure of 5 x 10^{-6} torr with a turbomolecular pump, back by a rotary mechanical pump.

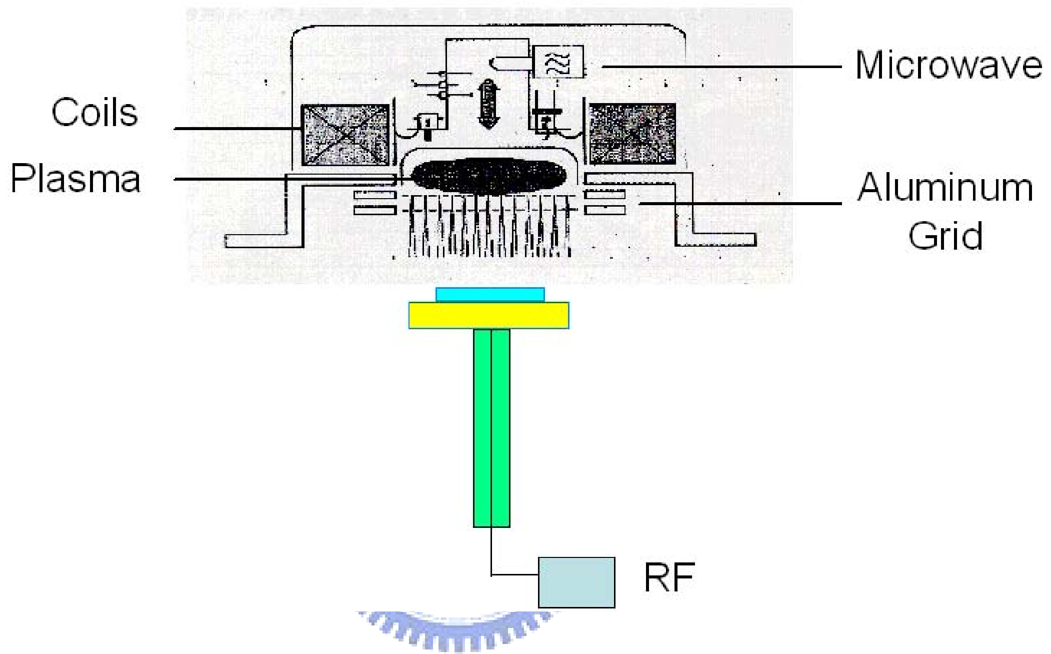

Figure 1-7 The schematic illustration of the ECR microwave plasma CVD system.

ECR plasma is generated by the microwave excitation of a 2.45 GHz frequency by a magnetron through a waveguide in a resonator volume. Through the Lorentzian force acting upon the electrons, the magnetic field causes the electrons to move along circular or spiral-shaped paths, as shown in figure 1-8. The anagular frequency of the electrons is proportional to the field intensity applied by the magnets. Microwave frequency and electron movement can be synchronized by setting the

suitable angular frequency. This results in maximum power absorption by the electrons from the alternating electric field of the microwaves, when the collision frequency of the electrons with neutral particles is lower than the excitation frequency. This means that the ECR effect can only be used at pressures below 10^{-1} to 10^{-2} mbar.

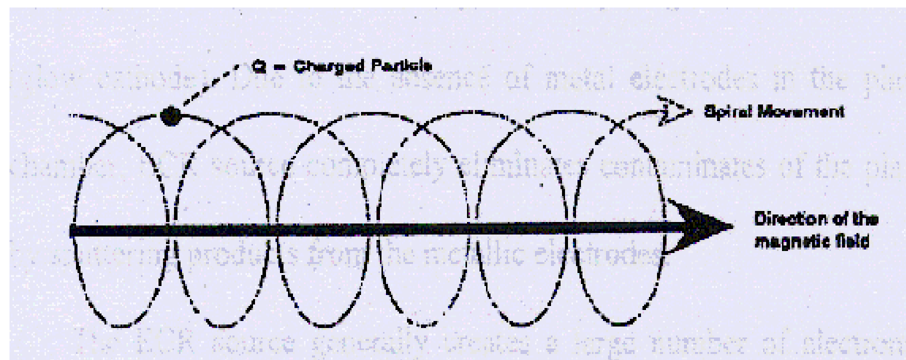

Figure 1-8 A charged particle is forces by magnetic field to move along a spiral path. ECR with reinforced plasma is obtained, if the spiral movement and the microwave field are synthesized.

The ECR source generally creates a large number of electrons to generate a high density of plasma. Hence, the total pressure for the ECR-CVD is much less than that for PECVD (Plasma-enhanced CVD). The required power is also much lower than that for PECVD. ECR-CVD thus provides a drastic reduction in the heat load transferred from the ion source to the substrate. Consequently, the induced plasma possesses lower ion energy, and the resulting film will achieve a higher quality due to low defect density. Because of the advantages of microwave ECR-CVD method

such as lower temperature, large area, lower ion damage, contamination-free and high deposition rate are good for chemical vapor deposition. Therefore we have prepared unbroken, large area, and flat fluorinated amorphous carbon films at room temperature in a short time. Moreover, the k-value can be controlled by the various flow ratios.

Reference

1 R. H. Havemann, M. K. Jain, R. S. List, A. R. Ralston, W-Y. Shih, C. Jin, M. C. Chang, E. M. Zielinski, G. A. Dixit, A. Singh, S. W. Russell, J. F. Gaynor, A. J. McKerrow, and W. W. Lee, Res. Soc. Symp. Proc., **511**, 1988, p3-14.

2 L. Peters, Semiconductor International, Sep. 1998, p84.

3 M. Rossnegal and D. Mikalsen, J. Vac. Sci. Technol. A, **9**, 261 (1991).

4 T. Sakurai, IEEE trans. Elec. Devices, **40**, 118 (1993).

5 I. Bunget and M. Popescu, Physics of Solid Dielectrics, Elsevier, 1984, p.207.

6 R. Waser, *Nanoelectronics and Information Technology*, Wiley-VCH, 2003.

7 R.P. Feynman, *The Feynmann Lectures on physics "Mainly Electromagnetism and Matter",* Calif. Addison-Wesley, Redwood City, 1989.

8 S.M. Sze, *Physics of Semiconductor Devices,* John Weily and Sons, New York, 1981.

9 R.C. Buchanan, *Ceramic materials for electronics: processing,*

properties, and applications, M. Dekker, New York, 1991.

10 J. O. Simpson and A. K. St Clair, Thin Solid Films **308**, 480 (1997).

11 H.O. Pierson, *Handbook of Chemical Vapor Deposition 2nd ed.*, Noyes, 1999.

12 M.L. Hitchman and K. F. Jensen, *Chemical Vapor Deposition*, Academic Press, 1993.

13 M.A. Lieberman and A. J. Lichtenberg, *Principles of Plasma Discharge and Materials Processing*, John Wiely & Sons, 1994.

Chapter 2

Literature Review

2-1 Low Dielectric Constant Materials

As integrated circuit dimensions continue to shrink, interconnected RC (resistance × capacitance) delay becomes an increasingly serious problem. In order to overcome the RC time delay, incorporating new materials of low resistivity and low permittivity into interconnected structure is one solution to replace the traditional Al and SiO_2. Copper is a substitute for aluminum in the future interconnection fabrication[1]. However, we do not know what kind of low dielectric constant (low k) material will replace the traditional SiO_2 or SiOF[2, 3], when a dielectric film requires a dielectric constant $k < 3.0$. The future low dielectric constant materials which support the semiconductor are illustrated by SIA roadmap (Fig. 2-1).

Year	1997	1999	2002	2005	2007	2010	2013
nm	250	180	130	80	65	50	35
K value	4	4.0-3.5	3.5-2.6	2.6-2.0	K < 2.0	K < 2.0	K < 2.0
Barrier	TiW, Ti/TiN	TiW, Ti/TiN	TiW, Ti/TiN	Ta, TaN, WN	Ta, TaN, WN	Ta, TaN, WN	Ta, TaN, WN
Wiring	Aluminum	Aluminum	Aluminum	Copper	Copper	Copper	Copper
Dielectric		SiO_2 and SiOCH	SiO_2 and SiOCH; Porous SiOCH	SiO_2 and SiOCH; Porous SiOCH	Porous SiOCH; Unknow?	Unknow?	Unknow?

Figure 2-1 summarizes the timeline of the materials anticipated in future generation multi-level interconnected structures. (Source: The International Technology Roadmap for Semiconductors: Update 2001)

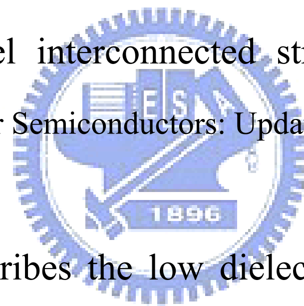

Table 2-1 describes the low dielectric constant materials for ULSI interconnection, and the basic requirements for low k materials are summarized in Table 2-2. The hydrogen silsesquioxane (HSQ) film and Methyl-silsesquioxane (MSQ) film which belong to SiOF base films were used in current 130 nm generation of semiconductor industry. So far maybe the k = 2.7 of black diamond film which belongs to SiOCH base film will be used in 90 nm generation of semiconductor industry. Future semiconductor devices in integrated circuits will soon be developed into a size as small as 45 nm generation, and maybe the porous SiOCH base film[4] will be applied in semiconductor industry. The basic mechanical properties of the Young's Modulus and hardness which are for semiconductor industry are about 12 GPa and 1.5 Gpa, respectively. The ultra low

dielectric constant materials must be lower than 2.0 for the next ULSI generation. Both porous silica (Xerogels/Aerogels) and PTFE polymer (Teflon) materials conform to the ultra low k requirement. The porous silica has high hardness and hydrophilic characteristic. These properties are disadvantageous for IC process integration of low k materials. The PTFE polymer has hydrophobic characteristic. PTFE films can be deposited by sputtering, but the sputtering yield is very low. The mixing of fluorocarbon and hydrocarbon gases produces fluorinated amorphous carbon (a-C:F) film by CVD methods. The a-C:F film properties are similar to PTFE. It accelerates the deposition rate and decreases the dielectric constant as well.

With its lower dipole moment[3] and lower electronic polarizability[5] properties, the C-F bonds have a large electronegativity, therefore considered ideal to construct low dielectric material. Savage et al. were the first one to deposit a-C:F film by plasma CVD in 1975[6], and Endo et al. were the first one who suggested fluorinated amorphous carbon thin film as a low dielectric constant material in 1995[7]. The permanent dipole moment of fluorinated carbon molecule is as low as 0.5[3], while the electronic polarizability of fluorocarbon bond is as low as 0.56[5]. Thus, the a-C:F film is an excellent low dielectric constant material.

Endo et al. used helicon plasma enhanced CVD to deposit a-C:F film[8]. This particular CVD brings up the deposition rate (0.15 ~ 0.3 μm/min), and accelerates the structural cross-linking in the film. Such network structure improves the thermal stability. All of the sp^3 bounds of PTFE polymer are linear CF_2 bonds, and the thermal stability temperature of PTFE polymer is as high as 200℃. However, some of network structure

is in the a-C:F film, and its thermal stability temperature can be over 300℃. Unfortunately the highly network structure of a-C:F film will cause the dielectric constant to grow. Endo et al.[9] and Yokomichi et al.[10] found that nitrogen atom can help to form the cross-linking in the a-C:F:N film, of which dielectric constant is ~ 2.4 until 400℃. If we increases the fluorinate concentration in a-C:F films, we can get ultra low dielectric constant (~1.5) in a-C:F films. And then we can use hydrogen or nitrogen plasma treatment to enhance the thermal stability. In addition, a-C:F film is an ultra low k film, the a-C:F film is also an excellent field emission material[11]. The work function of a-C:F film is ~0.012 eV. The a-C:F film has a lot of advantages. For example, the a-C:F film has high break-down voltage, hydrophobic property, and is easy for etching.

Table 2-1. Low dielectric constant materials for ULSI interconnection.

Dielectric	Dielectric constant	Glass transition temperature (Tg) (℃)	Refractive index	Water absorp. (%)	Stress (Mpa)	Gap Filling (μm)	Cure Temp. (°C)	Weight Loss (wt%)
FSG (silicon oxyfluoride, Si_xOF_y)	3.4-4.1	>800	1.42	<1.5	-130	<0.35	No issue	None
HSQ (hydrogen silsesquioxane)	2.9	>500	1.37	<0.5	70-80	<0.10	350-450	<3
MSQ (Methyl-silsesquioxane)	2.5-2.7	>500	1.36	<0.25	60-70	<0.10	400-500	<3
Nanoporous silica	1.3-2.5	>500	1.15	TBD	0	<0.25	400	none
Fluorinated Polyimides	2.6-2.9	>400	ΔRI>0.15(ai)	1.5	2	<0.5	350	<0.1
Poly(arylene)ethers	2.4-3.0	290		0.15			425	<1.0
Parylene AF4 (aliphatic tetrafluorinated poly-p-xylyene)	2.5	T_{melt}>510	1.548ΔRI >0.09(ai)		100	0.18	420-450	0.5
Fluorinated Poly(arylene)ethers (FLARE®)	2.4-2.7	175-265		0.2-1	30-50	0.1-0.8	450	0.5
Polyimides	3.2-3.6	>350	ΔRI>0.22(ai)	0.5-3.0				5-40
Aromatic hydrocarbon	2.65	>490	1.628	<0.25	55-6-	<0.05	400-450	<1.0
Bisbenzo(cyclobutene) BCB	2.6-2.8	$T_{dec.}$>350		0.23	85	<1	250	~1
PTFE (polytetrafluoro-ethylene) (Teflon®)	1.9	$T_{dec.}$>250-300	1.34	<0.01	25-27	<0.30	360-390	0.8
Hybrid-Silsesquioxanes	<3	$T_{melt.}$>250	1.58	0	30-40	<0.1	450	6
Xerogels/Aerogels	1.1-2.5	N/A				0.1	300-400	

Table 2-2. Basic requirements for low dielectric constant materials.

Requirements for Low-K Dielectrics	
Film Properties	**Manufacturing**
Dielectric constant: – Bulk: $k < 2.7$ – Effective: $k = 3.0 \sim 3.6$	Integration: – Good adhesion to metals (Ta, TaN, TiN, Cu), oxides/nitrides
Thermal stability: – High thermal conductivity – $Tg > 400°C$, stable above 425°C for short periods – Low expansion	– CMP compatible – High gap-fill and planarization – Minimize need for liner/capping films
Electrical properties: – High reliability – Leakage current: similar to SiO_2 – Breakdown field: similar to SiO_2 – Dissipation factor: <0.01 – Low charge trapping	– Etch selectivity to nitrides, oxides, oxynitrides – O_2 ash/solvent compatible
Film composition: – Low film stress – Low water absorption – High cracking resistance	– Avoid C_2H_6, C_3H_8 (CVD) – Avoid toxic solvents (spin-on dielectrics)

(Ref: Semiconductor International)

2-2 Fluorinated Amorphous Carbon

Fluorocarbon film was used as a surface coating in early stage because fluorocarbon film has lower frication and hydrophobic characteristics[12]. Even though the fluorocarbon films are always produced after chamber cleaning or silicon dioxide etching in semiconductor industry[13-16], but the fluorocarbon did not serve as low dielectric materials in integrated circuits, since the dielectric constant of silicon dioxide material was low enough for very large scale integrated (VLSI) device at that moment. However, when the semiconductor was promoted to the 180 nm ultra large scale integrate (ULSI) devices, the dielectric constant of low dielectric constant (low k) material must be lower than 3.0[17].

Therefore, there was a demand for new interlayer insulators to improve the switching performance of ultra-large-scale integrated (ULSI) devices. The need has led to intensive studies on several low-dielectric materials. Among them, fluorinated amorphous-carbon (a-C:F) films have received most attention due to their thermal stability and low dielectric constant[7, 18-24]. The relationship between these properties and the film compositions has been discussed in several studies[21-25]. The stability and dielectric properties could be manipulated by adjusting the F content of the films via control of the flow rate ratio of the source gases or by other techniques. A higher F concentration in the films normally reduces the thermal stability and the dielectric constant because it leads to weaker C-C cross linking, lower density and reduced polarization[26-28]. However, the films with high excess F, despite their thermal instability, have low leakage current and extremely high breakdown resistance. In a low

temperature environment, they could be applied as excellent insulating layers. In this thesis, we report on the structural and electrical properties of the high-F-content a-C:F films prepared by electron cyclotron resonance/chemical-vapor deposition (ECR-CVD).

In fluorocarbon plasma, it is well known that low F/C ratios of the precursor gases usually facilitate film growth, while high ratios induce erosion processes[29]. Previous studies on plasma CVD using CH_4 and CF_4 gases[18-24] showed that the deposition rate of a-C:F films first increases with the ratio of F/C, then declines rapidly from the maxima to zero, where the ratio was calculated in consideration of the total number of F atoms divided by the total number of C atoms in the inlet gas flux per unit time. Apparently, the growth rate of a-C:F films of high F content using the source gases of very high F/C ratio was limited by the etching effect of concentrated F radicals. On the other hand, a much higher deposition rate of a-C:H films by PECVD can be achieved by using C_2H_2 as a precursor rather than CH_4[30]. Therefore, CF_4 and C_2H_2 were employed as the source gases in this study to ensure a reasonable film growth rate.

The microwave plasma ECR-CVD system described in this thesis was used to produce reactive chemical species, and the RF bias assisted the precursor to impinge on the substrate, resulting in the deposition of the film. Both C_2H_2 and CF_4 were the precursors used for the synthesis of the a-C:F films. The C_2H_2 gas has a high C/H ratio, and could contribute enough carbon source to support a film network to increase the deposition rate[31]. The CF_4 gas has a high F/C ratio enough to supply sufficient fluorocarbons to raise the concentration of fluorine in the a-C:F film. The CF_4 plasma contains mainly CF_3^+ ions, F neutrals, CF_n radicals and negative ion species.

Fluorine atoms control not only the concentration of CF_n radicals through the gas-phase reactions but also the surface reactions[32-36].

In this thesis, we report on the chemical and physical properties of the fluorinated amorphous carbon film prepared by ECR-CVD, at CF_4 flow ratios from R = 0.90 to R = 0.98, where R is $CF_4/[CF_4+C_2H_2]$. This is to compare the difference between the as-deposited film and the film after annealing at 300^oC for 30 min. For this purpose we used the analytical instruments as follows: Fourier transform infrared absorption spectrophotometer (FTIR), electron spectroscopy for chemical analyzer (ESCA), high resolution electron energy loss spectrometer (HREELS), electron spin resonance spectrometer (EPR), photoluminescence spectrometer (PL), ultraviolet / visible spectrophotometer (UV/VI), field emission scanning electron microscope (FESEM), pulse laser spectrometer and atomic force microscope (AFM). Current-voltage (I-V) measurements were performed with the HP4156, and the capacitance (C-V) characteristic was measured at a frequency of 1MHz using the HP4280. The sp^2 content and the fluorine concentration would affect the photoluminescence lifetime, as well as energy band gap of the a-C:F films. With the rise of the temperature, the dangling bond density increases, resulting from the growing numbers of unpaired spins in the defects in the films.

Reference

1 C. R. Savage, R. B. Timmons and J. W. Lin, Adv. Chem. Ser., **236**, 745 (1993).

2 Kazuhiko Endo, Toru Tatsumi, J. Appl. Phys., **78**, 1370 (1995).

3 CRC Handbook of Chemistry and Physics. 77th Ed., CRC Press, Boca Raton (1996).

4 A. Grill and V. Patel, J. ElCh. Soc., **151**, F133 (2004).

5 K. J. Miller, J. Am. Chem. Soc., **112**, 8533 (1990).

6 K. G. Budinski, J. Vac. Sic. Technol. **12**, 786 (1975).

7 K. Endo, T. Tatsumi, J. Appl. Phys., **78**, 1370 (1995).

8 K. Endo and T. Tatsumi, Appl. Phys. Lett., **68**, 2864 (1996).

9 K. Endo and T. Tatsumi, Appl. Phys. Lett., **68**, 3656 (1996).

10 H. Yokomichi, and A. Masuda, J. Non-Cryst. Solids **271**, 147 (2000) 641.

11 S. H. Lai, K. P. Huang, Y. M. Pan, Y. L. Chen, L. H. Chan, P. Lin, and H. C. Shih, Chem. Phys. Let. **382**, 567 (2003).

12 C. R. Savage, R. B. Timmons and J. W. Lin, Adv. Chem. Ser., **236**, 745 (1993).

13 R. d'Agostino, R. Lamendola, P. Favia, and A. Giqel, J. Vac. Sci. Technol. A **12**, 308 (1994).

14 G. S. Oehrlein, Y. Zhang, D. Vender, and M. Haveriag, J. Vac. Sci. Technol. A **12**, 323 (1994).

15 M. J. Sowa, M. E. Littau, V. Pohray, and J. L. Cecchi, J. Vac. Sci. Technol. A **18**, 2112 (2000).

16 E. A. Joseph, B. Zhou, S. P. Sant, L. J. Overzet, and M. J. Goeckner, J.

Vac. Sci. Technol. A **22**, 689 (2004).

17 “The National Technology Roadmap for Semiconductors”, Semiconductor Industry Association, San Jose, CA, 1997.

18 H. Yokomichi, T. Hayashi, T. Amano and A. Masuda: J. Non-Cryst. Solids **227,** 641 (1998).

19 Y. Ma, H. Yang, J. Guo, C. Sathe, A. Agui and J. Nordgren: Appl. Phys. Lett. **72, 3353** (1998).

20 H. Yang, D. J. Tweet, Y. Ma and T. Nguyen: Appl. Phys. Lett. **73,** 1541 (1998).

21 J. A. Theil: J. Vac. Sci. & Technol. B **17,** 2397 (1999).

22 K. Endo and T. Tatsumi: Jpn. J. Appl. Phys. **36, L1531** (1997).

23 H. Yokomichi and A. Masuda: J. Appl. Phys. **86, 2468** (1999).

24 L. G. Jacobsohn, D. F. Franceschini, M. E. H. Maia da Costa and F. L. Freire, Jr. : J. Vac. Sci. & Technol. A **18, 2230** (2000).

25 T. W. Mountsier and J. A. Samuels: Thin Solid Films **332,** 362 (1998).

26 H. Yokomichi, T. Hayashi and A. Masuda: Appl. Phys. Lett. **72,** 2704 (1998).

27 K. Endo and T. Tatsumi: J. Appl. Phys. **86,** 2739 (1999).

28 J. P. Chang, H. W. Krautter, W. Zhu, R. L. Opila and C. S. Pai: J. Vac. Sci. & Technol. A. **17,** 2969 (1999).

29 J.W. Coburn and H. F. Winters: J. Vac. Sci. & Technol. **16,** 391 (1979).

30 P.S. Andry, P.W. Pastel and W. J. Varhue: J. Mater. Res. **11**, No.1

(1996) 221.

31 P. S. Andry, P. W. Pastel, and W. J Varhue, J. Mater. Res. **11**, 221 (1996).

32 G. Chuge and J. P. Booth, J. Appl. Phys. **85**, 3952 (1999).

33 W. Schwarzenbach, G. Cunge, and J. P. Booth, J. Appl. Phys. **85,** 7562 (1999).

34 K. Teii, M. Hori, M. Ito, T. Goto, and N. Ishii, J. Vac. Sci. Technol. A **18**, 1 (2000)

35 L. G. Jacobsohn, D. F. Franceschini, M. E. H. Maia da Costa, and F. L. Freire, Jr, J. Vac. Sci. Technol. A **18,** 2230 (2000).

36 K. Sasaki, H. Furukawa, K. Kadota, and C. Suzuki, J. Appl. Phys. **88,** 5585 (2000).

Chapter 3
Characterization Techniques for Fluorinated Amorphous Carbons Films

3-1 Introduction

For evaluating mechanical, electronic, chemical and physical properties of the a-C:F films, seventeen metrology tools were used to analyze them. The OES was used to detect the radicals of deposition plasma. The TDS was used to test the thermal stability of a-C:F films from 25℃ to 1050℃. The AFM and nano-indentor were used to detect the morphology and hardness of a-C:F films, respectively. The field emission scanning electron microscope (FESEM) was used to measure the thickness of a-C:F films. The composition and chemical states of the a-C:F films were analyzed by Glow Discharge Spectrometer (GDS)**,** Fourier-Transform infrared (FTIR) Spectrometer and X-ray photoelectron spectroscopy (XPS). The microstructure was evaluated by High-Resolution Transmission Electron Microscope (HRTEM). The sp^2/sp^3 bond ratio was obtained through high-resolution electron energy-loss spectroscopy (HREELS, Gatan, GIF 2000). The Electron Paramagnetic resonance (EPR) equipment was used to observe the dangling bound density in a-C:F films. Current-voltage (I-V) measurements were obtained by the HP4156, and the capacitance (C-V) characteristic was measured at a frequency of 1MHz using the HP4280. The n&k Analyzer, UV-Visible Spectrophotometer

(UV/VI), Photoluminescence (PL), Photoluminescence (PL), and Pulse Laser were used to evaluate the optic properties of a-C:F films.

3-2 Analyses and Measurements Techniques

3-2-1 Optical Emission Spectroscope (OES)

The OES was applied to characterize the composition of the plasma. The plasma precursor is diagnosed by using OES in the visible light range (200 ~ 800 nm) and Princetron Instrument Inc. Model ST121. Optical emission in the vicinity of sample surface in the microwave discharge was collected by an optical fiber and guided into the slit (10 μm) of a 0.5-m monochrometer (Acton Research Corporation Model Spectropro-500). Spectral scans from 200 to 800 nm were recorded as synthesis conditions varied. The OES is compatibly linked to a computer, programmed to obtain qualitative information on the radicals present and their dependence on the experimental conditions.

3-2-2 Thermal Desorption Analyze (TDA)

The TDA apparatus was employed to analyze the released gas from the sample during the thermal heating. Thermal stability was tested by TDA gas analysis system (MTM Engineering, WT268) with a quadrupole mass spectrometer which characterized the released gas of fluorinated carbon bonds from 25℃ to 1050℃, and the maxima measurement range of quadrupole mass were 200 amu..

3-2-3 Atomic Force Microscope (AFM)

AFM uses the interaction force between the probe and surface structure feature to measure the surface topography. The AFM tip diameter of Si_3N_4 cantilever (Microprobes, from Digital Instruments) was measured in a scanning electron microscope around 30-40 nm. To minimize any tip-induced damages, a contact force as small as possible, a set point of -20 (ca. 25-50 nN), was employed. The scan rate was 1.5 Hz. Calibration for the in-plane length measurements was carried out with a diffraction grating whereas the height was calibrated using a series of VLSI standards. The surface topography and roughness of a-C:F films were examined by atomic force microscope (Digital instrument NS3a controller with D3100 stage).

3-2-4 Nano-Indentor

The nano-indentor (Hysitron, Hysitron 35) was used to measure hardness of the fluorinated amorphous carbon films. The Berkovich diamond tip was used to test a-C:F films' hardness. In order to avoid the substrate effect, the thickness of a-C:F films were deposited as thick as 1.5 μm.

3-2-5 Field-Emission Scanning Electron Microscope (FESEM)

The thickness of the a-C:F films were measured by field-emission scanning electron microscope (FESEM, Hitachi S-5000, Japan) with a resolution 2nm. Comparing FESEM with α-step and n&k , the FESEM thickness data of a-C:F films are more accurate.

3-2-6 Glow Discharge Spectrometer (GDS)

The GDS apparatus has ppm level resolution. GDS (GDS750A, ECO,

U.S.A.) was used to characterize whether the hydrogen element exists in a-C:F films or not.

3-2-7 Fourier-Transform Infrared Spectrometer (FTIR)

FTIR is the most widely used analytic method for the molecular structure characterization of organic and inorganic compounds. The types of fluorinated carbon bonds were measured by FTIR. All samples were qualitatively analyzed by FTIR (BOMEN Model DA8.3 SNV), and the scan ranged from 500 to 4000 cm^{-1} with a 2cm^{-1} resolution. The infrared light transmitted through the sample at normal incidence and then through a KBr grating into the MCT detector. The absorption spectrums of a blanket Si is used as the background signals.

3-2-8 X-ray Photoelectron Spectroscope (XPS)

Of all the contemporary surface characterization methods, XPS is most widely used. XPS is also called electron spectroscopy for chemical analysis (ESCA). Surface analysis by XPS is accomplished by irradiating a sample with monoenergetic soft X-ray and analyzing the energy of the detected electrons. The XPS measurements were carried on Perkin Elmer model PHI 1600 by using a single Mg Kα X-ray operating at 250 W. The X-ray source is at an angle of 54.7^o with respect to the analyzer. Peak energy positions were corrected by using Pt peak. Based on the result from the high-resolution spherical capacitor analyzer (SCA), the energy resolution is 1.0 eV as survey scan spectrum and 0.1 eV as core-level spectrum, respectively. We used XPS chemical shift to make the C-C, CF, CF_2, and CF_3 bonds certain quantities.

3-2-9 High-Resolution Transmission Electron Microscope (HRTEM)

HRTEM is the most powerful equipment for material microstructure analysis. The nanostructures were investigated by high-resolution transmission electron microscopy (HRTEM, JEOL, JEM-2010F and).

3-2-10 High-Resolution Electron Energy Loss Spectroscope (HREELS)

The electronic structures of fluorinated amorphous carbon film were investigated by high-resolution energy loss spectroscope. HREELS (Gatan, GIF 2000, U.S.A.) was used to characterize sp^2% in the a-C:F films. The energy resolution is 0.1 eV to characterize 1s → π* transition in a-C:F films.

3-2-11 Electron Paramagnetic resonance (EPR)

The dangling bonds of a-C:F films were measured by EPR. We used EPR (Bruker, EMX-10, Germany) to observe the dangling bond density from 4K to 423K. The central magnetic field is ~3400 Gauss, and the microwave is ~9.5 GHz.

3-2-12 Capacitance-Voltage (C-V) Curve

The dielectric constants of all the films were estimated according to the capacitance-voltage (C-V). The capacitance (C-V) of a-C:F films was measured at 1 MHz by HP4280 apparatus. The mask with a diameter of 250 μm was covered on a-C:F films. For the C-V measuring, the top and bottom electrodes of Pt layer were coated with the mask by the MIM structure (Pt/a-C:F/Pt).

3-2-13 Current-Voltage (I-V) Curve

The current-voltage characteristic of a-C:F films was observed by HP4156 at a voltage from 0 to 100V. The sample structure is MIM structure, too.

3-2-14 n&k Analyzer

The refractive index of a-C:F films were measured by n&k analyzer (n&k Technology, n&k analyzer 1200, U.S.A.), with the wavelength ranging from 190 to 1000 nm.

3-2-15 UV-Visible Spectrophotometer (UV/VI)

The optical transparence of a-C:F films was examined by HP8453 UV/VI (U.S.A.) spectrophotometer, with the wavelength ranging from 190 to 1100 nm.

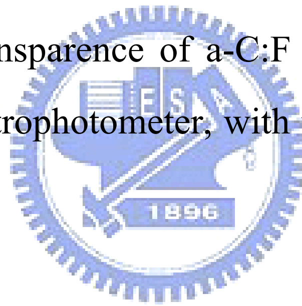

3-2-16 Photoluminescence (PL)

The fluorescence was observed by a fluorescence photoluminescence (PL) apparatus with helium-cadmium (He-Cd) laser (λ = 325 nm) as an excitation source.

3-2-17 Pulse Laser

Excimer pulse laser (Lamda Physik, Mode LPX 150P, λ=193 nm) was applied to measure photoluminescence lifetime of a-C:F films. The record time unit is 10^{-8} second.

Chapter 4

Synthesis and Characterization for Physical and Chemical Analysis

4-1 Introduction

In this work, ECR-CVD equipped with a rf bias in the chamber mixing acetylene (C_2H_2) and tetrafluoromethane (CF_4) gases was used to prepare a-C:F film on the silicon or 7059 glass substrate. Electron cyclotron resonance chemical vapor deposition (ECR-CVD) could provide many advantages, like high density plasma, high planarity, deposition on large area, and low temperature process. Unlike SOG process, there is no moisture generated during the preparation. The acetylane (C_2H_2) plasma has high C/H ratio which helps to grow a-C:H film structure rapidly[1,2]. The tetrafluoromethane plasmas present mainly CF_3^+ ions, F neutrals, CF_n radicals and negative species. F atoms control not only the concentrations of CF_n radicals through gas-phase but also surface reactions[3-7] in the plasma.

In this thesis, we report on the physical and chemical properties of the fluorinated amorphous carbon film prepared by ECR-CVD at various flow ratio R, where R is $[CF_4]/\{[CF_4+C_2H_2]\}$. The relationships between the properties of the films and the mixing ratio R are as follows.

4-2 Experiment

The flowchart figure 4-2 shows the measurement methods of chemical and physical properties.

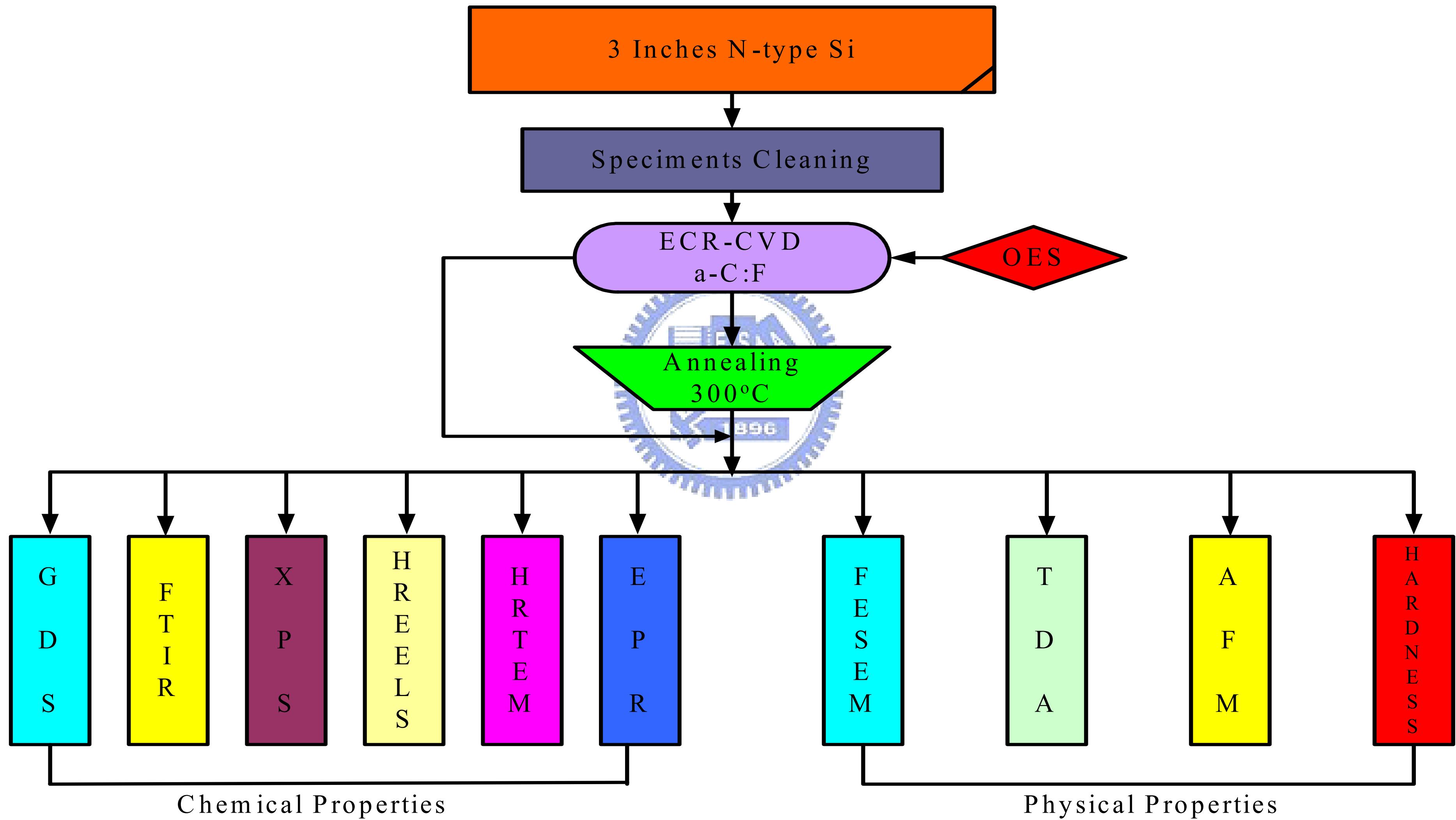

Figure 4-2 shows the measurement methods of chemical and physical Properties.

4-3 Sample Preparation

4-3-1 Substrate Cleaning

The n-type (100) 3-inch-diameter silicon wafers were used as the substrate material in this study. The silicon wafers were cleaned with standard RCA cleaning process in a wet bench (SCP, Santa Clara Plastics, U. S. A.). The RCA cleaning procedure has three major steps:

I. Organic Cleaning: Removal of insoluble organic contaminants with a 5:1:1 H_2O:H_2O_2:NH_4OH solution.

II. Oxide Strip: Removal of a thin silicon dioxide layer where metallic contaminants may accumulate as a result of (I), using a diluted 50:1 H_2O:HF solution.

III. Ionic Cleaning: Removal of ionic and heavy metal atomic contaminants with a solution of 6:1:1 H_2O:H_2O_2: HCl.

The RCA cleaning technique does not attack silicon, and only a very thin layer of silicon dioxide is removed (in II) in the process. The procedure was also designed to prevent the metal contaminants from coming back to the wafer's surface. When finished, the polished side should be like speculum without any residue.

4-3-2 Low k Film Deposition

We used RF bias assisted ECR-CVD to deposit the low k a-C:F films in this study. The RF (13.56 MHz) bias was fixed at -200V, and the microwave (2.45 GHz) power was fixed at 600W. Figure 4-3 illustrates a schematic configuration of the microwave ECR microwave plasma CVD system. The C_2H_2 and CF_4 were used as the plasma precursor. The CF_4 flow rate was fixed at 100 sccm, and the C_2H_2 flow rate was varied from 2

to 10 sccm. We controlled the base pressure below 5 x 10^{-6} torr, and then we deposited the a-C:F films at 2 x 10^{-2} torr working pressure. The temperature of the samples is the direct plasma temperature.

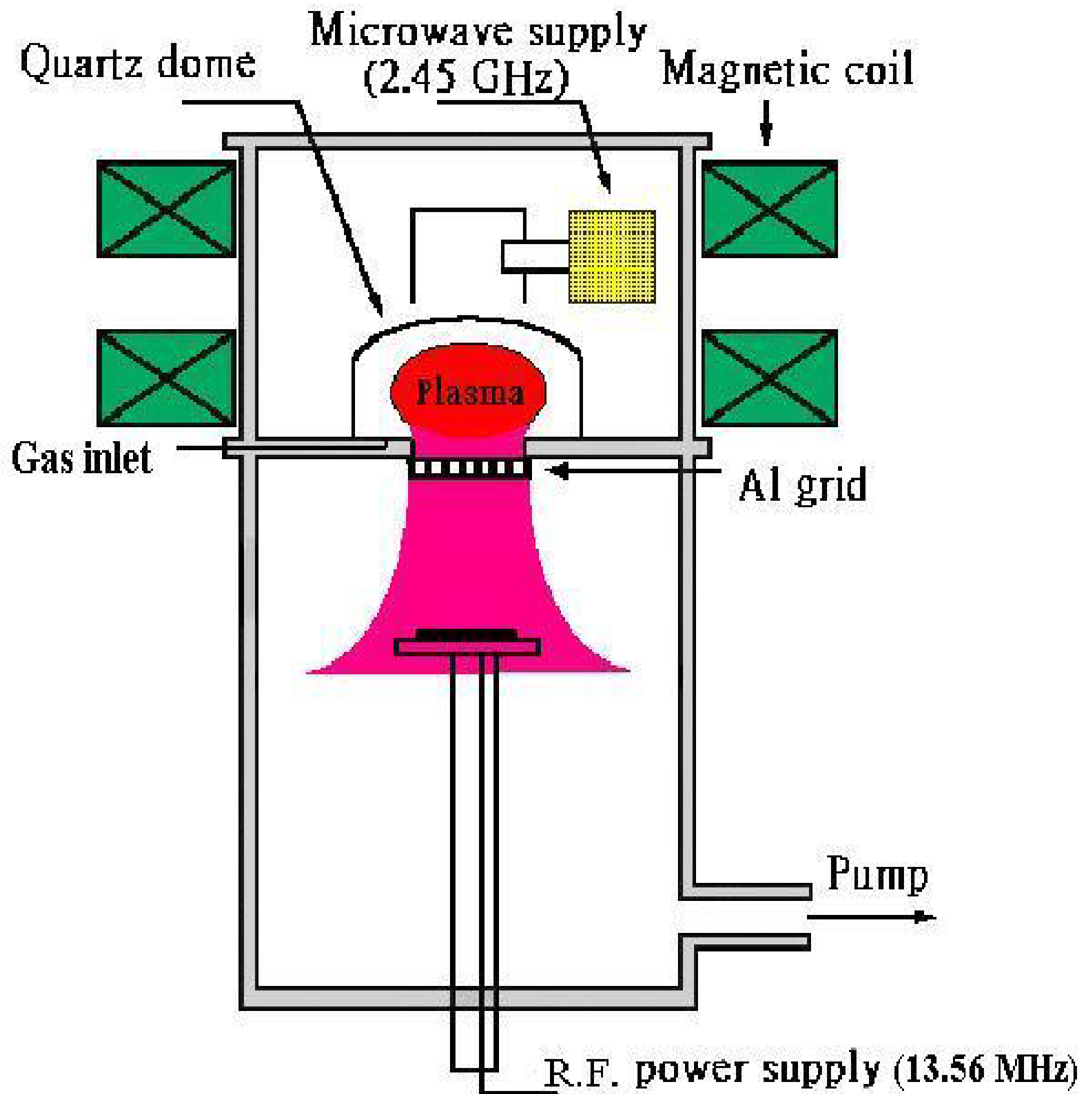

Figure 4-3 illustrates of the ECR microwave plasma CVD system.

Figure 4-3 shows the illustration of the ECR microwave plasma CVD system.

4-3-3 Annealing

The a-C:F films were annealed at 300℃ in pure nitrogen atmosphere (Carbolite Furnace CTF 12/05/550) for 30 minutes. The velocity for increasing and decreasing temperature is +/- 3 ℃/min.

4-4 Physical Analysis

The plasma composition states were examined, using optical emission spectroscopy (OES), with the visible light range of 200-800 nm. The film thickness was measured by FESEM in the as-deposited and after annealing condition, respectively. The TDS was used to evaluate the thermal stability of a-C:F films, and the test temperature is from 25℃ to 1050℃. We monitored the gas released from thermal decomposition, and the monitoring molecular weight is from 1 amu. to 200 amu.. The film morphology was observed with a Digital Instrument NS3a Controller at a D3100 stage AFM while the hardness was measured by a Nano Scope E Hysitron 35 from Digital Instruments.

4-5 Chemical Analysis

The a-C:F films were deposited directly on Si wafers. GDS and FTIR instruments were used to examine the quality of chemical compositions and bonds. XPS, HRHEELS and EPR instruments were used to examine the quantity of compositions, electronic structures and dangling bonds of a-C:F films. HRTEM was used to observe the a-C:F film nano-structure.

Reference

1 P. S. Andry, P. W. Pastel, and W. J Varhue, J. Mater. Res. **11**, 221 (1996).

2 Kyu Chang Park, Jong Hyun Moon, Jin Jang, and Myung Hwan Oh, Appl. Phys. Lett., **68,** 3594 (1996).

3 G. Chuge and J. P. Booth, J. Appl. Phys. **85**, 3952 (1999).

4 W. Schwarzenbach, G. Cunge, and J. P. Booth, J. Appl. Phys. **85,** 7562 (1999).

5 Kungen Teii, Masaru Hori, Masafumi Ito, Toshio Goto, and Nobuo Ishii, J. Vac. Sci. Technol. A **18**, 1 (2000)

6 L. G. Jacobsohn, D. F. Francesschini, M. E. H. Maia da Costa, F. L. Freir, and Jr, J. Vac. Sci. Technol. A **18,** 2230 (2000).

7 K. Sasaki, H. Furukawa, K. and Kadota, C. Suzuki, J. Appl. Phys. **88,** 5585 (2000).

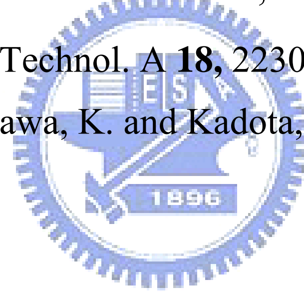

Chapter 5

Physical Properties

5-1 Introduction

Fluorinated amorphous carbon (a-C:F) films were deposited by RF bias assisted microwave plasma electron cyclotron resonance chemical vapor deposition (ECR-CVD) with tetrafluoromethane (CF_4) and acetylene (C_2H_2) as precursors. The deposition process was performed at flow ratios from R = 0.90 and R = 0.98, where R = CF_4/(CF_4+C_2H_2). The substrate temperature after finishing deposition was around 50°C, according to the thermal couple placed under the substrate. The thickness of as-deposited films ranged from ~ 400 Å (for R = 0.98) to ~ 700 Å (for R = 0.90). Subsequent annealing treatments of the deposited a-C:F films were carried out at 300°C for 30 min in pure nitrogen atmosphere. The higher flow ratio R led to lower deposition rate, and the hardness of a-C:F films decreased with uprising flow ratio R. The radicals of plasma were detected by OES equipment. AFM, nano-indenator and TDS were used to observe the morphology and thermal stability of a-C:F films, and FESEM was used to measure the film thickness in as-deposited condition and after annealing.

5-2 Result and Discussion

The plasma composition depends on various chemical pathways in the plasma, which again depends on the plasma parameters such as microwave power, RF power, electron temperature, electron density, gas

flow rate, and degree of ionization. To illustrate how these collisions could result in the radical production, Table 5-1 shows a set of reactions which is the possible sheath radical production in the C_2H_2 and CF_4 plasma[1-5]. The flow rate of the source gases were kept at flow ratio R (R = $CF_4/[(CF_4+C_2H_2)]$), 0.90, 0.95, 0.97 and 0.98. Figure 5-1 shows the optical emission spectra (OES) of the ECR excitation plasma at R = 0.90 and 0.97. There were C_2, C_3, CF_2, CH, F_2, H_2 and HF radical species, and C_2^-, F_2^+ and HF^+ ionic species in the plasma[6]. The C_2 radicals will construct the main skeleton of the a-C:F films, and the fluorine atoms will be replaced by hydrocarbons to form fluorocarbon bonds or HF bonds. Figure 5-2 shows CF and CF_2 species found in the plasma with the spectra for the wavelength range 200-300 nm. The F_2, F_2^+, CF, CF_2 and CF_3 radicals are both sinks and sources[7] at the same time during the deposition of the a-C:F films.

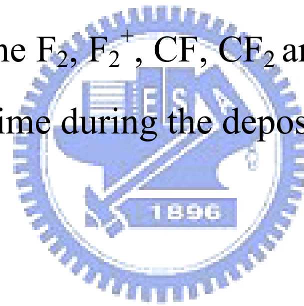

Table 5-1. Primary electron collisions

Process	Potential (eV)	Apparent Product
H^+	$e^- + C_2H_2 \rightarrow H^+ + H + C_2 + 2e^-$	20.8
	$\rightarrow H^+ + H + CH + C + 2e^-$	22.8
C^+	$e^- + C_2H_2 \rightarrow C^+ + 2H + C + 2e^-$	24.5
CH^+	$e^- + C_2H_2 \rightarrow CH^+ + CH + 2e^-$	22.2
C_2^+	$e^- + C_2H_2 \rightarrow C_2^+ + 2H + 2e^-$	23.8
	$\rightarrow C_2^+ + H_2 + 2e^-$	18.2
C_2H^+	$e^- + C_2H_2 \rightarrow C_2H^+ + H + 2e^-$	17.8
C_2H^+	$e^- + C_2H_2 \rightarrow C_2H_2^+ + 2e^-$	11.2
$C_2H_2^+$	$e^- + C_2H_2^+ \rightarrow C_2H + H$	-7.3
	$e^- + C_2H_2^+ \rightarrow C_2 + 2H$	-3.2
	$e^- + C_2H_2^+ \rightarrow 2CH$	-3.1
C_3H^+	$CH^+ + C_2H_2 \rightarrow C_3H^+ + H_2$	22.9
$C_3H_2^+$	$CH^+ + C_2H_2 \rightarrow C_3H_2^+ + H$	21.3
$C_4H_2^+$	$C_2^+ + C_2H_2 \rightarrow C_4H^+ + H$	19.2/22.5
$C_4H_2^+$	$C_2^+H_2^+ + C_2H_2 \rightarrow C_4H_2^+ + H_2$	11.38
$C_4H_3^+$	$C_2^+H_2^+ + C_2H_2 \rightarrow C_4H_3^+ + H$	11.07
CF^+	$CF_3^+ + CF_4 \rightarrow CF^+ + 2F$	8.08
CF_3^+	$CF^+ + CF_4 \rightarrow CF_3^+ + CF_2$	0.3
	$CF_3^+ + CF_4 \rightarrow CF_4^+ + CF_3 \rightarrow CF_3^+ + F + CF_3$	6.2
	$C^+ + CF_4 \rightarrow CF_3^+ + CF$	-1.78
	$e^- + CF_3^+ \rightarrow CF_2 + F$	-6
	$e^- + CF_3^+ \rightarrow CF + 2F$	-2.3
C^+	$CF^+ + CF_4 \rightarrow C^+ + CF_4 + F$	5.59

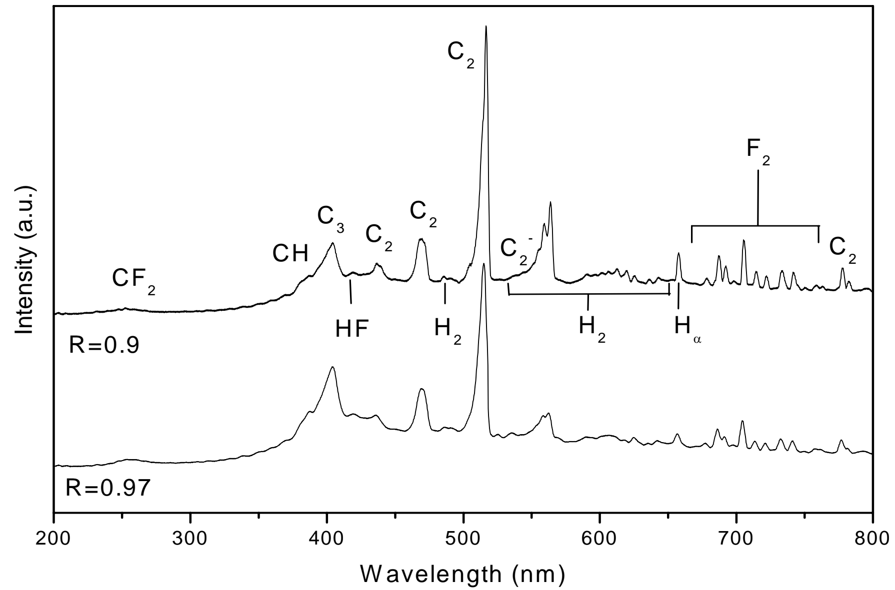

Figure 5-1. Optical emission spectra obtained in C_2H_2 and CF_4 mixed gas discharge at 600W source power -200V rf bias, and 20 m Torr in the ECR-CVD.

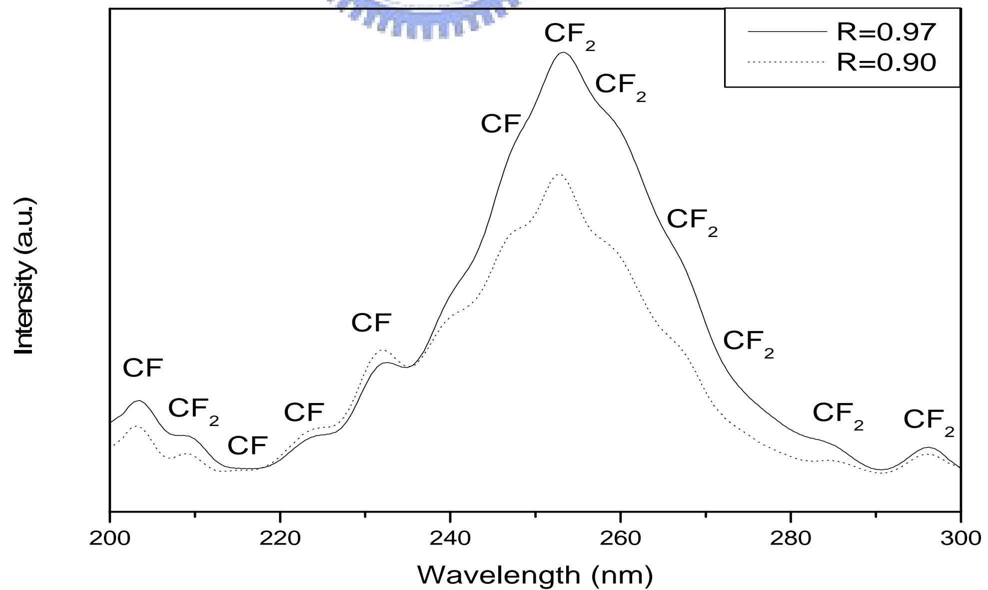

Figure 5-2 Comparisons of the plasma optical emission spectra for R = 0.97 and R = 0.90.

HRSEM was used to measure the thickness of a-C:F films. The behavior of the deposition rate as a function of the flow ratio of the CF_4/C_2H_2 gas mixture is presented in Figure 5-3. A steep decline in the deposition rate from 56 to about 3 nm/min was observed as the flow ratio increased from ~ 0.90 to ~0.98. This indicates that the etching effect of F radicals strengthens rapidly in the narrow region. The thermal desorption of the fragments in the a-C:F films is one of the major factors causing film shrinkage. The film thickness loss is proportional to the flow ratio R (Fig. 5-4) in a fashion similar to that of F concentration in the films, a result consistent with the lower thermal stability for the films of higher F content. Besides outgassing effect, the concurrent film structure relaxation during heat treatment may also induce shrinkage. The evolution of film microstructures, in particular, the voids observed in the films of high F content, would contribute to the change of thickness. Since the higher fluorine concentration a-C:F film has more sp^3 bounds in the film, it results in thermal instability at high temperature. The TDA result of R=0.90 a-C:F film is shown in Figure 5-5. No hydrocarbon molecular signals were found in the TDA result. There were only CF, CF_2 and CF_3 gases which terminated the carbon skeleton in the films released from the film during heating process.

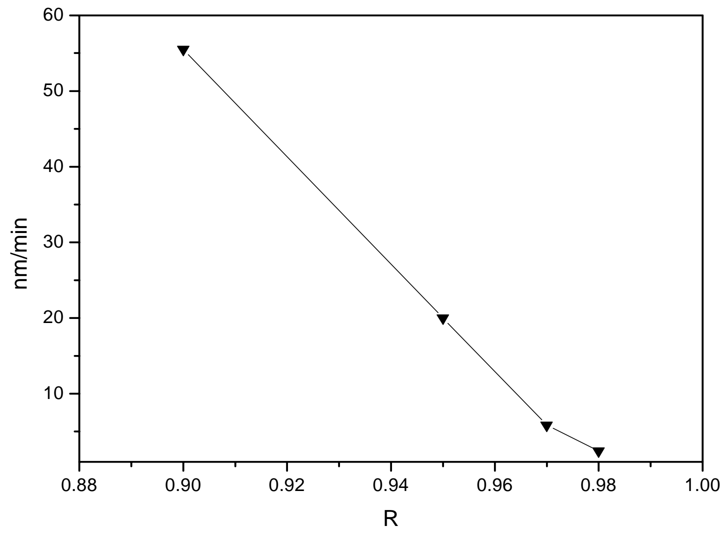

Figure 5-3 shows the deposition rate of a-C:F films.

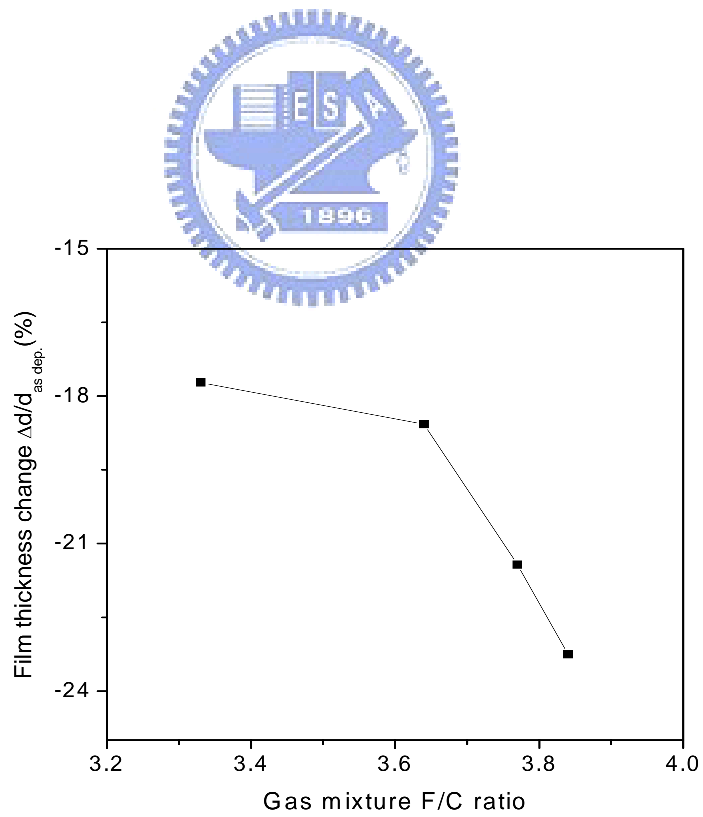

Figure 5-4. The shrinkage of film thickness is negatively proportional to flow ratio R

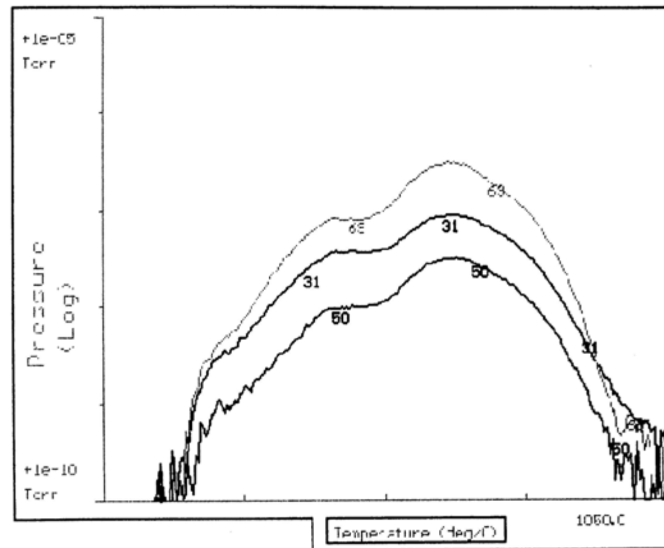

Figure 5-5 shows the TDA result of R = 0.90 a-C:F film. 31, 50 and 69 mean the molecule weight of CF, CF_2 and CF_3.

The topography of a-C:F films can be observed by AFM, as shown in Figure 5-6, and the surface roughness (root mean square) of the a-C:F films prepared by ECR-CVD is less than 0.8 nm, which is good for mechanical and electric applications. The relevant data are listed in table 5-2. The hardness of a-C:F films is also shown in Figure 5-7, and the a-C:F films is softer than copper film (~ 1 GPa). The higher flow ratio generates more linear fluorocarbon bonds, which will be annihilated after annealing. In contrast, the cross-linking bonds will be increased when the flow ratio is reduced. Consequently, the hardness of the a-C:F film depends on the fluorine content and the thermal treatment. Therefore the higher CF_4 flow ratio (R=0.98) produced more sp^3 linear structure, which made the a-C:F films smoother and softer.

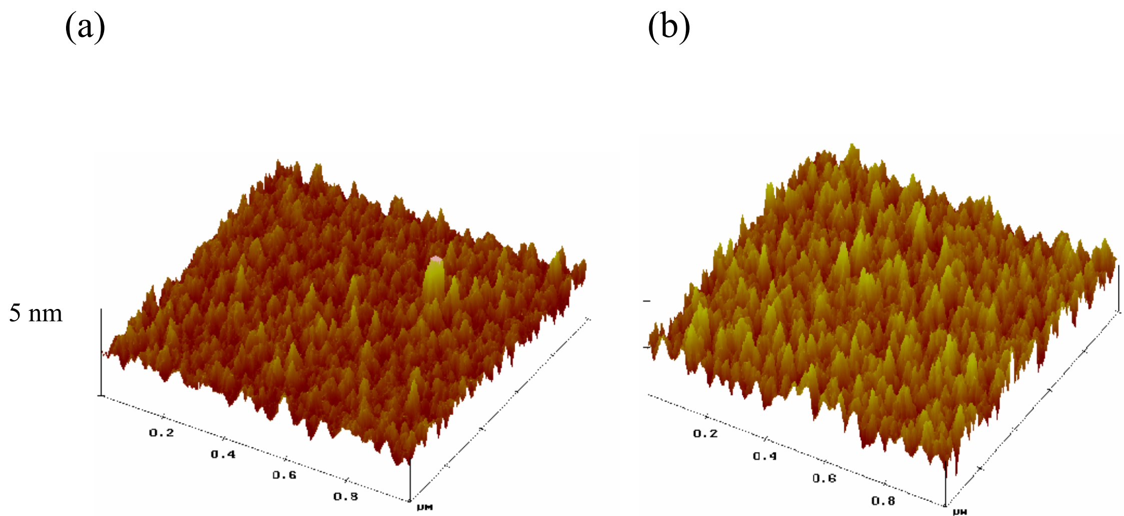

Figure 5-6 shows the AFM images of R = 0.90 a-C:F films. (a) is as-deposited, and (b) is after annealing.

Table 5-2. The hardness of a-C:F films in as-deposited and after annealed conditions.

	Roughness (nm)
R = 0.90 as-deposited	0.78
R = 0.90 after annealed	0.79
R = 0.95 as-deposited	0.60
R = 0.95 after annealed	0.76
R = 0.97 as-deposited	0.43
R = 0.97 after annealed	0.47
R = 0.98 as-deposited	0.42
R = 0.98 after annealed	0.47

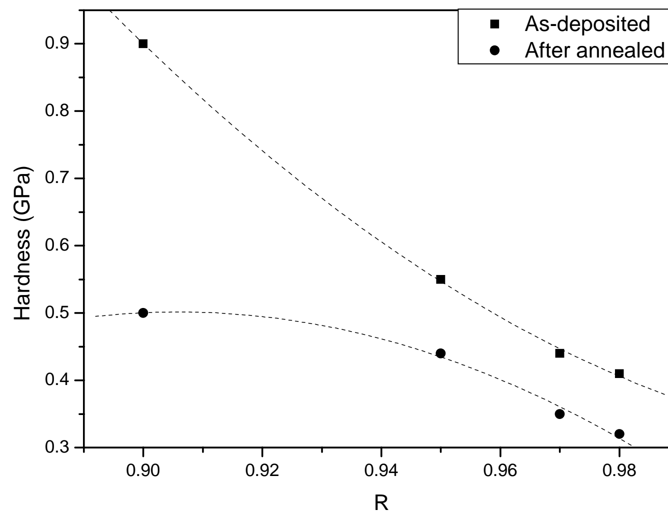

Figure 5-7 shows the hardness of the a-C:F films in as-deposited and after annealed condtions.

5-3 Summary

The a-C:F films of high fluorine content were obtained by the ECR-CVD method with tetrafluoromethane (CF_4) and acetylane (C_2H_2) as precursor gases. The ECR-CVD can get flat a-C:F film, and it is important to evaluate the dielectric constant of a-C:F films. The mechanical properties of a-C:F film depend on the plasma precursors. The fluorine concentration of a-C:F film increases with flow ratio R, and the higher flow ratio will form more linear fluorocarbon bounds in the film. As a result, at a higher flow ratio, the a-C:F films will have smoother and softer structure. The fluorocarbon molecules of a-C:F films will be released, starting at 150 ℃, and the a-C:F films will be entirely destroyed around 1000℃. With fluorine atoms replaced by hydrocarbons to form fluorocarbon bonds or HF bonds, no hydrocarbon molecular signals will be found in TDA results.

Reference

1 M. Stacey, Advances in Fluorine Chemistry, Butterworths: Washington, 1965.

2 F. H. Field and J. L. Franklin, Electron Impact Phenomena and the properties of gaseous ions, Academic Press, New York, 1970.

3 R. J. M. N. Snijkers, Ph. D. thesis, Eindhoven University of Technology, The Netherlands, 1993.

4 J. W. A. M. Gielen, M. C. M. van de Sanden, and D. C. Schram, Thin Solid Film, **271,** 56 (1995).

5 M. Weiler, S. Sattel, T. Giessen, K. Jung, H. Ehrhardt, V. S. Veerasamy and J. Robertson, Phys. Rev. B, **53,** 1594 (1996).

6 R. W. B. Pearse, and A. G. Gaydon, The Identification of Molecular Spectra (Fourth Edition), Wiley, New York, 1976.

7 Da Zhang, and M. J. Kushner, J. Vac. Sci. Technol. A **18,** 2661 (2000).

Chapter 6

Chemical Properties

6-1 Introduction

The glow discharge spectrometer (GDS) is used to measure, by ppm level, the quantities of elements in the samples. With this equipment we didn't find any hydrogen atom in the a-C:F films. The kinds of composition and bonds were observed by X-ray Photoelectron Spectroscope (XPS) and Fourier-Transform infrared (IR) absorption. XPS and IR measurements revealed that, after annealing, the strength of the CF and CF_3 bonds configuration is weaker than that of the CF_2 bonding configuration. The HREELS is the most reliable method of quantifying the sp^2 bond fraction. The a-C:F films often comprise a combination of two types of bonding: sp^3 and sp^2 type hybridizations. With the EPR equipment to measure the dangling bonds in the a-C:F films, we evaluate the electric properties in the films. The dangling bond defects give rise to states around the Fermi level, which is important in electronic materials as the dangling bond defects usually control the carrier recombination regardless of the states being either diamagnetic or paramagnetic. With the temperature on the rise, the dangling bond density increases, resulting from the growing numbers of unpaired spins in the defects in the films. The higher flow rate results in higher fluorinate concentration and more sp^3 bonds in the films. Moreover, the higher fluorinate concentration can stabilize the dangling bond density of the a-C:F films.

6-2 Result and Discussion

GDS is used to detect whether the films developed has hydrogen element or not. We found from GDS result that there is no hydrogen element signal in our films.

FTIR is a powerful instrument to probe the chemical structure of the a-C:F film, and it can detect a film as thick as ~1 μm. Figure 6-1 compares the as-deposited a-C:F films IR spectrum in different flow ratios. A summary of the absorption peaks is shown in Table 6-1[1-4]. We find that the infrared absorption counts rise at a positive rate with fluorine concentration. The R=0.98 a-C:F film presents clearly all infrared absorption spectrum of the fluorocarbon bonds. However, the FTIR intensity in R=0.90 a-C:F film is weaker than R=0.98. It only present infrared absorption spectrum of the CF_x (x=1, 2, 3) group and little C=C and CF_2 complex in the films.

Figure 6-2 shows the FTIR spectroscopy of the a-C:F films prepared at R = 0.97 and R = 0.90. There are only vibrating absorbance peaks of the fluorocarbon bonds, without those of any hydrocarbon bonds on the spectrum. It indicates that all of the hydrogen atoms reacted with fluorine atoms during the plasma reactions, which consequently formed HF species. The obvious difference between R = 0.97 and 0.90 is that the a-C:F films formed at R = 0.90 do not have CF_3 980 cm^{-1} absorption peak. The major peaks of the a-C:F film (R = 0.97) are $–CFCF_3$, CF_2 and C=CF stretch peaks, whereas the major peaks of the a-C:F film (R = 0.90) are CF_2 and C=CF stretch peaks. The peak intensity of each as-deposited a-C:F film is stronger than that of each film after annealing (at 300 ^{o}C). Moreover, Figure 6-2 shows that the intensity of the peaks for the after-annealed film

is lower than that for the as-deposited film from 730 to 1350 cm^{-1}, which implies that there are plenty of CF_2, CF_3 and CF-CF_3 bonds that will be broken in the film after annealing. However, the spectra of the a-C:F films prepared at R = 0.90 are almost the same in both conditions: as-deposited and after annealing. So the structure of the R = 0.90 film is more stable than that prepared at R = 0.97.

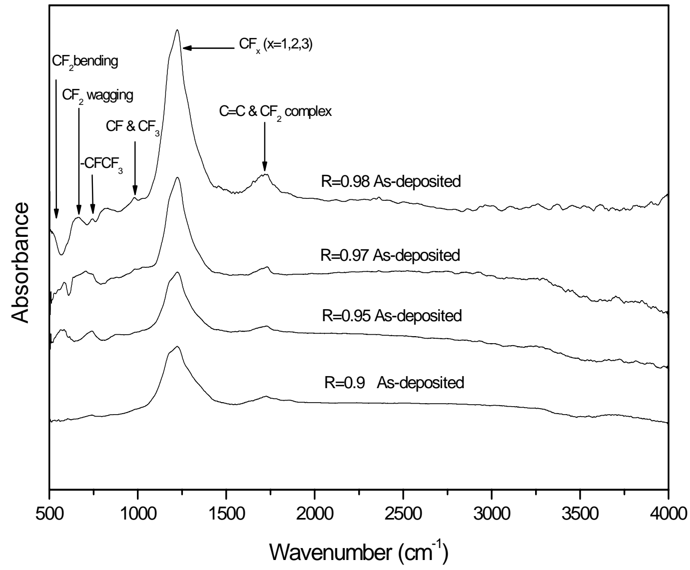

Figure 6-1 Comparing the FTIR spectrums of as-deposited a-C:F films at different flow rates.

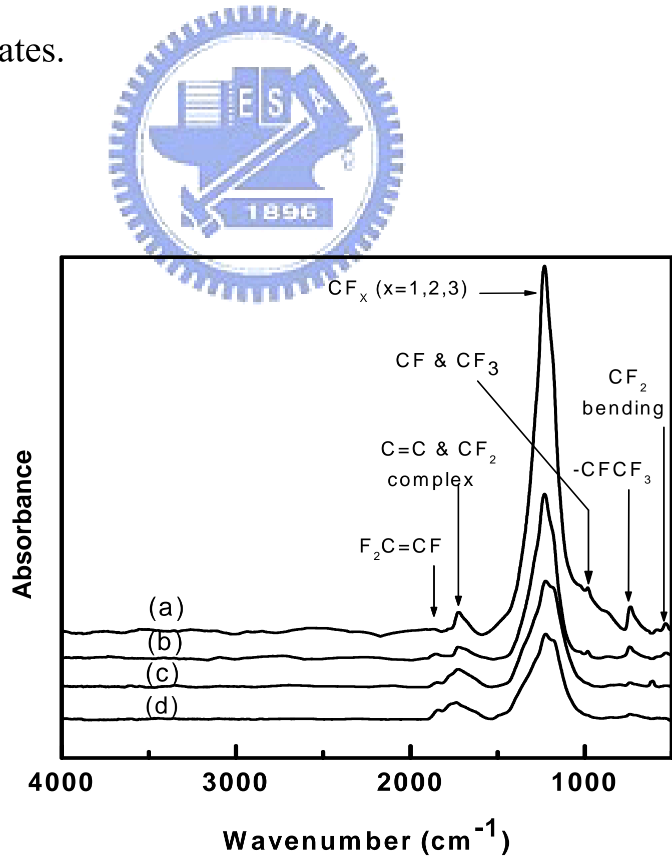

Figure 6-2. FTIR spectroscopy of the a-C:F film, (a) as-deposited at R = 0.97, (b) after being annealed at R = 0.97, (c) as-deposited at R = 0.90, (d) after being annealed at R = 0.90.

Table 6-1. Summary of FT-IR absorption peaks.

Wave number (cm^{-1})	**Assignment**
505	CF_2 rocking
553	CF_2 bending
635	CF_2 wagging
730-745	CF- CF_3
980	CF_3
1030 and 1070	CF
1120-1350	CF_3 group
1160	CF_2 symmetric stretch
1220 and 1450	CF_2 asymmetric stretch
1300-1340	CF= CF_2
1325-1365	CF_3CF_2
1340	CF stretch
1608-1700	C=CF stretch
1700	C=C stretch
1720	$F_2C=C<$
1860	$F_2C=CF$

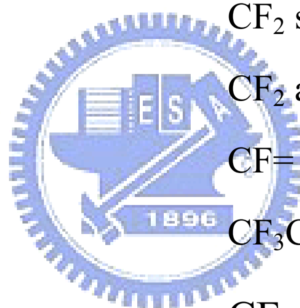

XPS is another powerful instrument for detecting the chemical structure of the a-C:F films, and is also a surface sensitive instrument providing only the local chemical bonds of the first ~50Å of the thin film. The C 1s spectrum of a-C:F film could be deconvoluted into five Gaussian peaks corresponding to CF_3 (293.2eV), CF_2 (290.95eV), CF (288.8eV), C-CF_x (286.5eV), and C-C or C-H (284.9eV), as shown in Figure 6-3. The absolute binding energies of CF_3, CF_2, CF, C-CF_x and C-C fall within the range, as listed in published literature[5-11] , valuing from 292.6 to 294, 290.3 to 292, 287.8 to 289.3, 285.5 to 287.3, and 283.4 to 285 eV, respectively. From the deconvoluting of the C 1s spectrum, fluorine-to-carbon ratios (F/C) can easily be calculated by the distribution of the integrated intensities of the various components of the C 1s spectrum[12], according to

$$F/C = (3I_{CF3} + 2I_{CF2} + 1I_{CF}) / I_{C\ 1s} \quad (1)$$

where I_{bond} is the photoemission intensity (i.e. area under each Gaussian curve) originating from a specific bond. The chemical composition of the a-C:F samples, in the as-deposited state and after annealing at 300°C for 30

min respectively, were estimated by XPS and displayed in Fig. 6-4. The results show that the molar fraction of fluorine increases with the flow ratio R, finally reaching ~55 at% at R = 0.98. Also, all of the samples lose fluorine after annealing due to thermal decomposition, and the loss of the F content increases with flow ratio R, revealing the low thermal stability of the films with high F content. The hydrogen concentration in the films was found to be negligible since no C-H stretching was observed in the FTIR spectra.

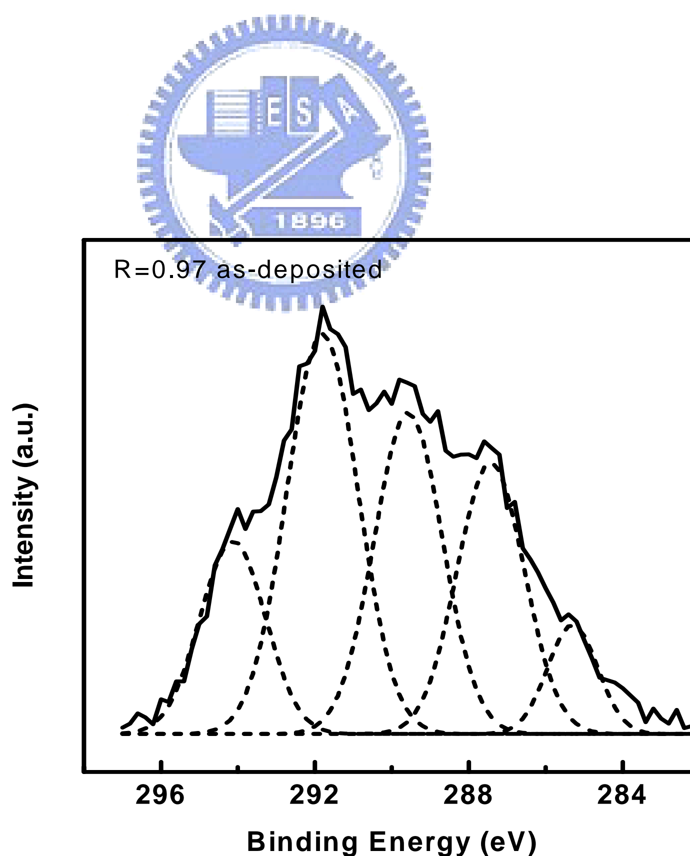

Figure 6-3. Deconvoluted C 1s spectrum of a-C:F film at R = 0.90

as-deposited obtained by XPS analysis.

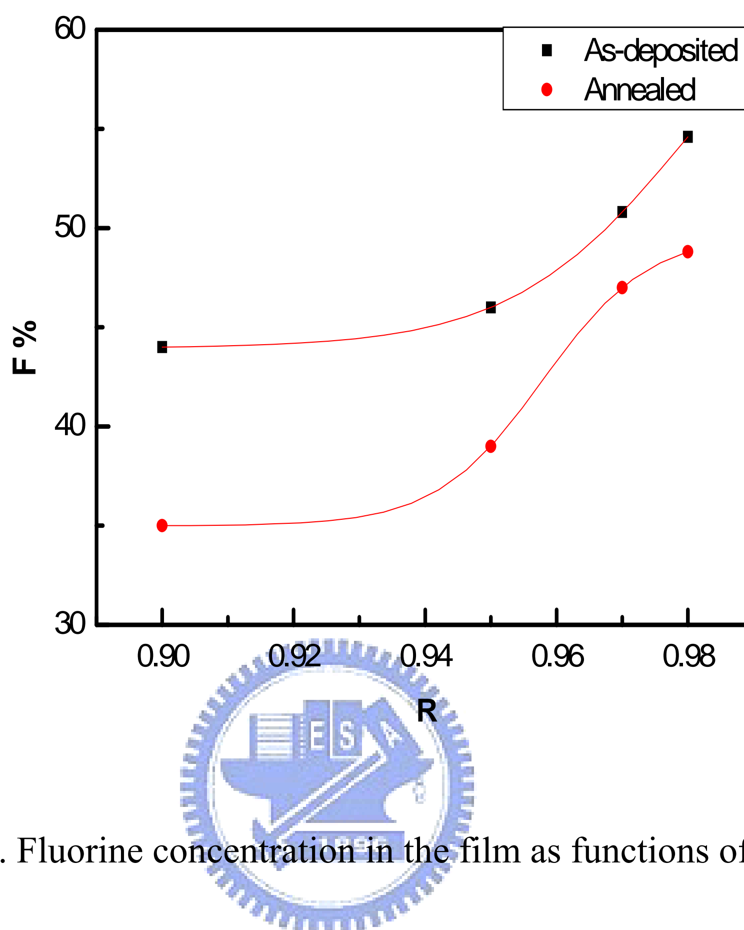

Figure 6-4. Fluorine concentration in the film as functions of flow ratios.

XPS survey spectra of the a-C:F samples were taken from the film surface rather than from inside the film body, since the pre-sputtering required in the latter process would cause preferential sputtering of F and would change the true chemical state of the film within the detected area[13]. Five components, C-C, C-CF_x, CF, CF_2 and CF_3, deconvoluted from the C 1s photoemission spectra, are shown as a function of flow ratios in Fig. 6-5. These components are associated with the various bonding environments of carbon atoms. It has been reported that the C-C cross-linked structure provides the thermal stability of the film, while the

CF_x (x=1,2,3) components, particularly CF_2 and CF_3, reduce the degree of cross-linking and the corresponding stability[14,15]. Hence, the declining amount of C-C bonding configurations found in the films of high R ratio (Fig. 6-5) is consistent with the inferior thermal stability characteristics, as suggested by the higher thermal loss in F content for these films (Fig. 6-4).

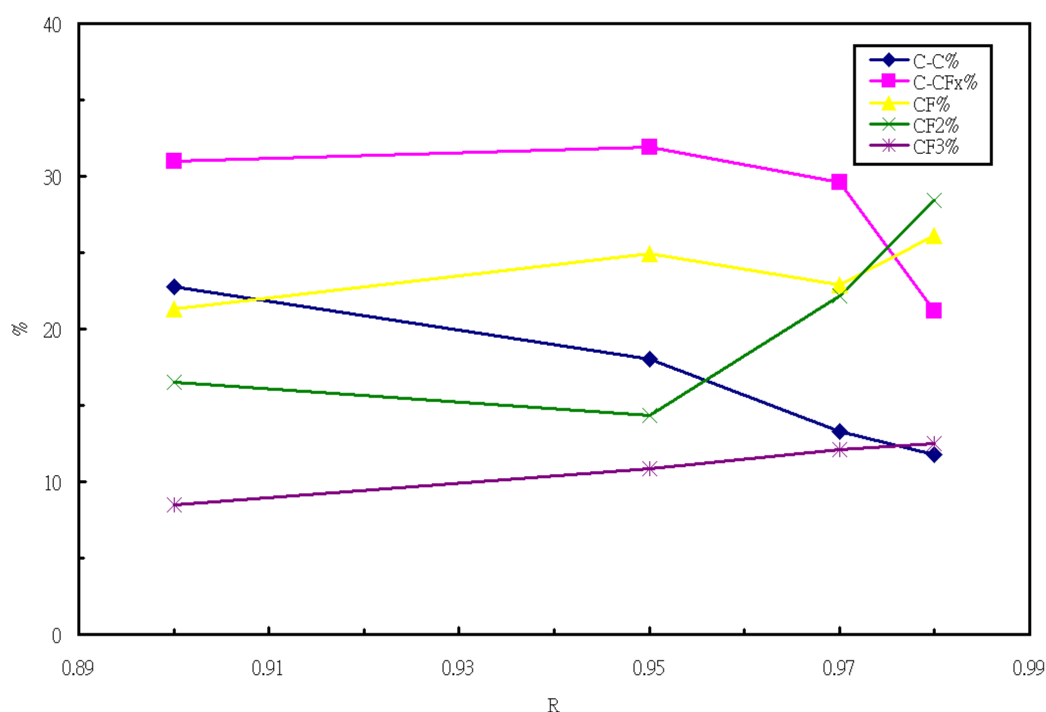

Figure 6-5. Change in C 1s spectra of the as-deposited a-C:F films as functions of the flow ratios. The integrated intensities of the C 1s spectra are normalized.

Figure 6-6 and Table 6-2 show the results from the C 1s spectrum deconvolution. The fluorine concentration of the R = 0.97 a-C:F film is higher than that of the R = 0.90 film, and the major peak of the R = 0.97

a-C:F film is the C-CFx and CF bonds in both as-deposited and after-annealed conditions. In contrast to the CF_2 bond of R = 0.97 a-C:F film, the C-CFx bond of R = 0.90 film is the main peak in the as-deposited condition and the C-C bond is the main peak after annealing. The mass of the C-C bond falls as the CF_4 flow ratio rises. When we increase the flow ratio R, the CF_2 concentration will significantly grow. Evidently, the C 1s deconvolution varies in both R = 0.97 and 0.90 a-C:F films in as-deposited and after-annealed conditions. The peak areas for C-CFx, CF, CF_2 and CF_3 shrink with the R = 0.90 a-C:F film being annealed, but the amount of the C-C peak area increases relatively. The peak areas for CF, CF_2 and CF_3 decrease when the R = 0.97 a-C:F film is annealed, but the C-C and C-CFx peak areas increase relatively. This is because the a-C:F film will break a lot of weaker bonds in the a-C:F film, and release fluorocarbon molecules during annealing. Consequently, the fluorine concentration will decrease after the a-C:F film is annealed.

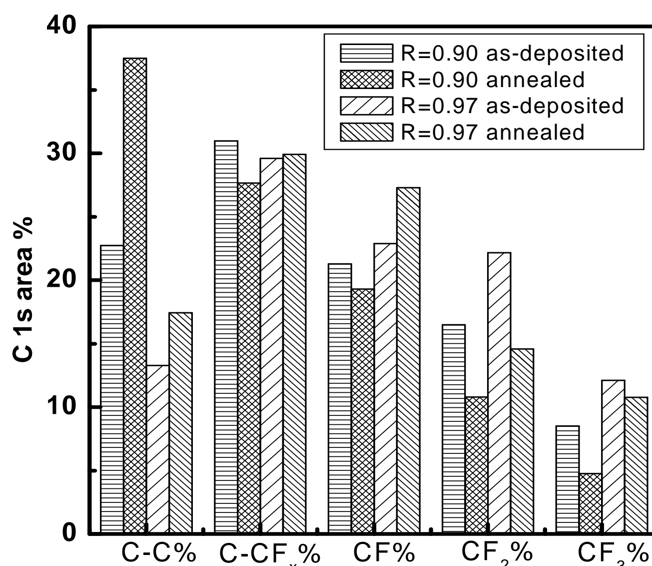

Figure 6-6. Deconvolution result of the a-C:F film C 1s spectrum for R = 0.97 and R = 0.90 in the as-deposited and after annealing conditions obtained by ESCA analysis.

Table 6-2. ESCA chemical composition (at. %) of the a-C:F films in as-deposited and after annealing (at 300°C) conditions.

CF_4 Flow ratio	C-C	C-CF_x	C-F_1	CF_2	CF_3	F%
R=0.97 (as-deposited)	13.3	29.6	22.9	22.1	12.1	50.8
R=0.97 (after annealed)	17.4	29.9	27.3	14.6	10.8	47.0
R=0.90 (as-deposited)	22.7	31.0	21.3	16.5	8.5	44.4
R=0.90 (after annealed)	37.5	27.6	19.3	10.8	4.8	35.6

The HREELS is the most reliable method of quantifying the sp^2 bond fraction. The a-C:F films often comprise a combination of two types of bonding: sp^3 and sp^2 type hybridizations. The bonding types can be analyzed by the K-shell electron-energy-loss (EELS) spectrum of C 1s. Figure 6-7 shows the HREELS spectra in the carbon K-edge region after being removed from the background. The steep rise at 287.4 eV in the 100% sp^3 bonds of diamond spectrum corresponds to the onset of the 1s → σ^* transitions, and the peak position at about 285eV corresponds to surface dangling bonds and/or to defects in the crystal. The graphite spectrum, which is 100% sp^2 bonds structure, shows a clear peak at 285 eV and a steep rise at 289.4 eV corresponding to the 1s → π^* and to the onset of 1s → σ^* transitions, respectively[16,17]. The a-C:F film spectrum almost matches with that of diamond-like carbon (a-C or a-C:H) [16-18]. Moreover, both the fluorinated amorphous carbon and diamond-like carbon films are sp^3 and sp^2 mixed structures.

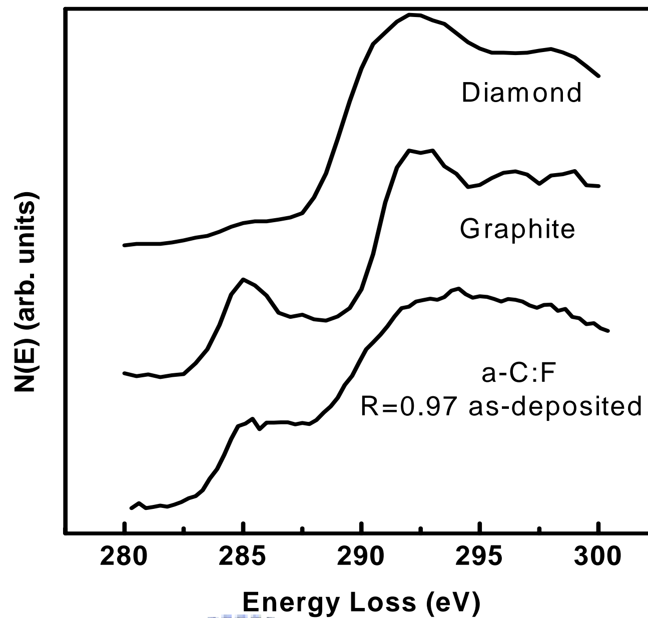

Figure 6-7. Comparisons of the HREELS spectra in the carbon K-edge region.

The method for qualifying the sp^2 bonding fraction in the a-C:F film from the electron-energy-loss spectra is described by Berger and McKenzie[16]. Here, the area under the 1s → π* peak of the a-C:F film is normalized to a energy window, referring to an equivalent ratio for graphite, which has 100% sp^2 bonding. The mathematical principle of quantifying the edge is to obtain a ratio of the two areas, one of which is the standard, as shown in the following formula:

$$f = \frac{I_{g\pi*}\, I_u(\Delta E)}{I_{u\pi*}\, I_g(\Delta E)} \quad (2)$$

where f is the ratio between the two π* peaks, $I_{\pi*}$ is the integral 1s → π* transition of graphite, and $I(\Delta E)$ is the integrated counts for the normalizing energy windows. The superscripts g and u denote the graphite and unknown spectra respectively.

Figure 6-8 shows the carbon K-edge fitting of the R = 0.97 as-deposited amorphous carbon films. There are three Gaussian peaks in the spectra which are centered at 285, 287, and 293 eV, and these peaks indicate the 1s → π* transition, the molecular transition, and 1s → σ* transitions respectively[16, 19-21]. Figure 6-9 shows the sp^3% of as-deposited and after-annealed a-C:F films. The sp^3 fraction rises with a positive rate in CF_4 flow ratio R. At higher CF_4 flow ratios, more fluorine atoms are supplied, each of which can be incorporated as a single F atom bonded to carbon, which is similar to the H atom in its ability to stabilize the dangling bond in amorphous carbons[22]. It is therefore generally believed that the fluorine atom is helpful to the increase of the sp^3 bonding component in a-C:F film. Furthermore, the sp^3 fraction decreases when the a-C:F film is subject to annealing. The sp^3 bonds of the diamond-like carbon (DLC)

belong to a metastable phase[23-25], so the magnitude of sp^2 bonds of the a-C:F film will be enlarged after annealing. As the hardness of a-C:F films is lower than that of stiff a-C:H film, it is believed that, in the a-C:F films, most of the sp^3 bounds are in linear structure while the rest is in network structure. In addition, the sp^3 bounds in network structure in as-deposited films are more than those in the after annealing films, as the sp^3 bounds are transferred to soft sp^2 bounds during annealing. With such large quantities of sp^3 bonds in diamond-like film, the hardness is usually over 20 GPa[27-29].

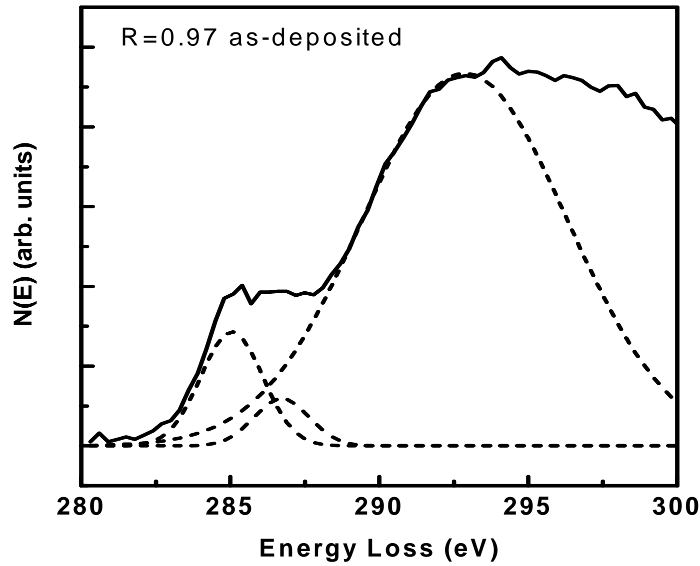

Figure 6-8. The spectra for carbon K-ionization edge obtained from R = 0.97 as-deposited. The fitting lines were obtained using three Gaussian peaks centered at 285, 287, and 293 eV.

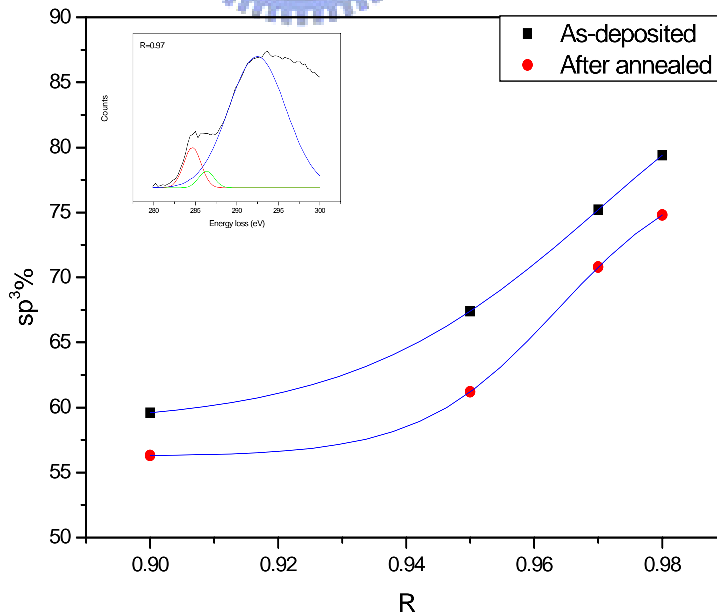

Figure 6-9 shows the sp^3 % of as-deposited and after annealing a-C:F films.

In addition to the outgassing effect, the concurrent film structure

relaxation during heat treatment may also induce shrinkage. The evolution of film microstructures, in particular, the voids observed in the films of high F content, would contribute to the change of thickness. The subsequent annealing induced the shrinkage of these light regions and the formation of dark regions as seen in Fig. 6-10. The local change in the contrast of image, following the direction of the electron beam, primarily relates to local fluctuation in the effective film thickness,. In the featureless amorphous background, some nano-sized light regions are evident, which can be described as density-deficient regions or voids[30]. The dark regions were verified to be carbon-rich clusters by carbon element mapping using HREELS. In addition to the thermal decomposition of CF_x components previously described, nano-void shrinkage is also expected to reduce the film thickness after annealing, but their quantitative contribution has not been estimated. It is noted that the heat treatment not only boosted the C-C cross-linking of the films, but also induced an inhomogeneous distribution of C-rich regions on the nano-scale demonstrated in Fig. 6-11.

(a) (b)

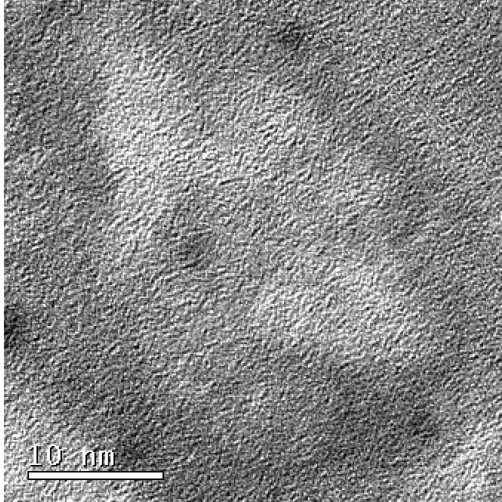

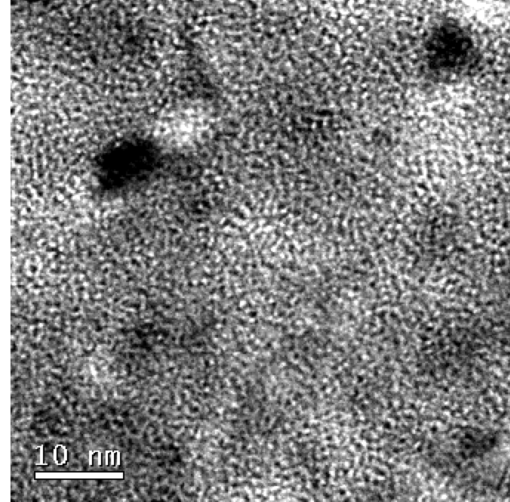

Figure 6-10. (a) is the HRTEM image of the R = 0.98 as-deposited film, and (b) is of the one after annealing.

1896

(a) (b)

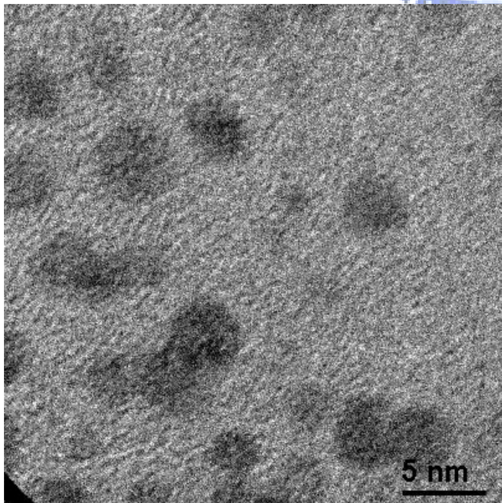

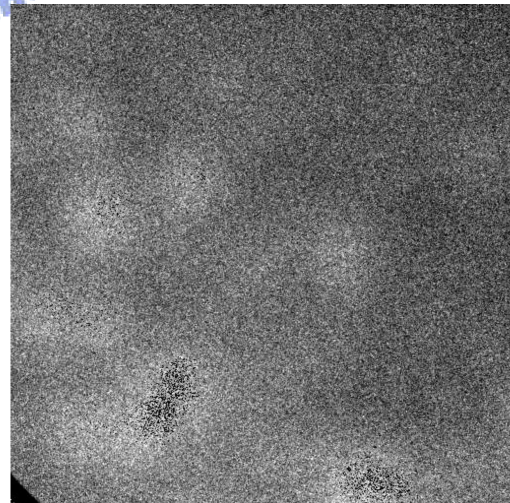

Figure 6-11. (a) is the HRTEM image of R = 0.95 a-C:F film after annealing , and (b) is the HREELS image by carbon element mapping of same film.

The dangling bond defects give rise to states around the Fermi level, which is important in electronic materials as the dangling bond defects usually control the carrier recombination regardless of the states being either diamagnetic or paramagnetic[21]. The density of paramagnetic defects can be measured by EPR. The range of dangling bond densities of a-C:F films at R = 0.97 and R = 0.90 as-deposited is ~ $2x10^{19}$ - $5x10^{20}$ spins/cm^3 from 4K to 423K. However, after being normalized by the Curie's law, the range of dangling bond densities is ~ $5.5x10^{18}$ – $5.5x10^{19}$ as shown in Fig. 6-12. The hopping rate of a dangling bond electron is lower at the reduction of temperature[31]. As the temperature rises, the number of unpaired spins will grow considerably due to the electron hopping from the defects. Furthermore, numerous nano-voids in the a-C:F film[32] will enhance the density of dangling bonds with the rise of temperature. The higher fluorine concentration leads to lower density of dangling bonds in the a-C:F film, which means that the fluorine atoms and ions can easily react with the dangling bonds of the carbon frame during the CVD deposition. In addition, after annealing the a-C:F films, the leakage current at a higher flow ratio would be lower than that at a lower flow ratio[32]. The details will be discussed in next chapter.

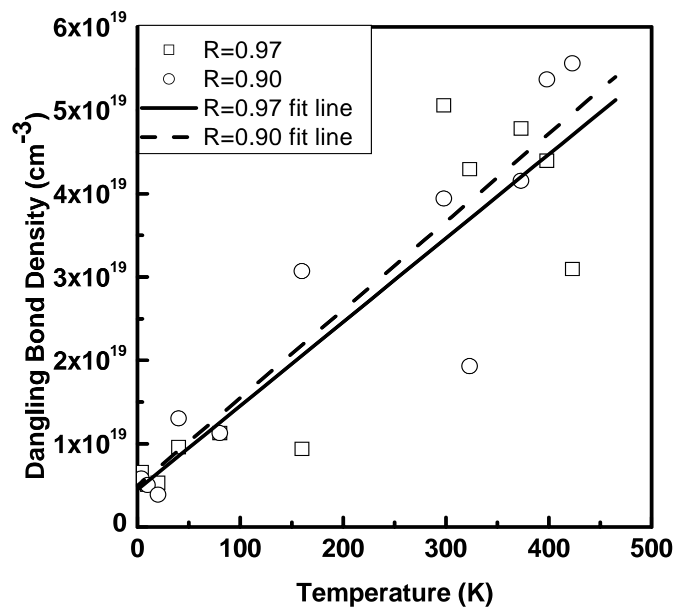

Figure 6-12. The density of dangling bonds of the a-C:F films at R = 0.97 and R = 0.90 as deposited.

6-3 Summary

The sp^3 bond ratio and fluorine concentration will go up with the fluorocarbon flow ratio on the rise. The FTIR and XPS results reveal that the structure of the a-C:F films differentiates when films are prepared with various CF_4 flow ratios. Furthermore, the result of EELS reveals that annealing of the films helps to multiply the carbon double bond structures in the a-C:F films. The higher CF_4 flow ratios generate more sp^3 linear structures, and help to smooth and soften the a-C:F film. There is a lot of structural variation after annealing; therefore, the electrical and optical properties of the a-C:F films are different from these of the as-deposited films. We will discuss those phenomenon in next two chapters. The

higher fluorine concentration helps to lower density of dangling bonds in the a-C:F films, while the nano-voids in the films enhance the density at rise of temperature.

Reference

1 Norman B. Colthup, Lawrence H. Daly, and Stephen E. Wiberley, Introduction to Infrared and Raman Spectroscopy (Third Edition), Academic Press, Boston, Ch. 12 1990.

2 M. Inayoshi, M. Hori, T. Goto, M. Hiramatsu, M. Nawata, and S. Hattori, J. Vac. Sci. Technol. A **14,** 1981 (1996).

3 D. C. Marra, and E. S. Aydil, J. Vac. Sci. Technol. A **15**, 2508 (1997).

4 H. Yokomichi, and A. Masuda, Vaccum. **59,** (2000) 771.

5 M. A. Butler, R. J. Buss, and A. Galuska, J. Appl. Phys. **70**, 2326 (1991).

6 K. Endo and T. Tatsumi, J. Appl. Phys. **78**, 1370 (1995)

7 A. M. Hynes, M. J. Shenton, and J. P. S. Badyal, Macromolecules. **29**, 4220 (1996).

8 S. F. Durrant, S. G. C. Castro, L. E. Bolívar-Marinez, D. S. Galvão, and M. A. B. de Moraes, Thin Solid Films **304,** 149 (1997).

9 Y. Ma and H. Yang, J. Guo, C. Sathe, A. Agui, and J. Nordgren, Appl. Phys. Lett. **72**, 3353 (1998).

10 M. Schaepkens, T. E. F. M. Standaert, N. R. Rueger, P. G. M. Sebel, G.

S. Oehrlein, and J. M. Cook, J. Vac. Sci. Technol. A **17,** 26 (1999).

11 S. Agraharam, D. W. Hess, P. A. Kohl, and S. A. Bidstrup Allen, J. Vac. Sci. Technol. A **17,** 3265 (1999).

12 R. d'Agostino (Ed.), Plasma Deposition, Treatment, and Etching of Polymers, Academic Press, Boston, 1990, p146.

13 N. Ariel, M. Eizenberg, Y. Wang and S. P. Murarka: Mater. Sci. Semicond. Proc. **4,** (2000) 383.

14 H. Yokomichi, T. Hayashi and A. Masuda: Appl. Phys. Lett. **72,** 2704 (1998).

15 J. P. Chang, H. W. Krautter, W. Zhu, R. L. Opila and C. S. Pai: J. Vac. Sci. & Technol. A. **17,** 2969 (1999).

16 S. D. Berger, D. R. McKenzie, and P. J. Martin, Philos. Mag. Lett. **57,** 285 (1988).

17 R. G. Pregliasco, G. Zampieri, H. Huck, E. B. Halac, M. A. R. de Benyacar, and R. Righini, Appl. Sur. Sci. **103**, 261 (1996).

18 P. J. Fallon, V. S. Veerasamy, C. A. Davis, J. Robertson, G. A. J. Amaratunga, W. I. Milne, and J. Koskinen, Phys. Rev. B, **48**, 4777 (1993).

19 A. P. Hitchcock, D. C. Newbury, I. Ishii, J. Stöhr, J. A. Horsley, R. D. Redwing, A. L. Johnson, and F. Sette, J. Chem. Phys. **85,** 4849 (1986).

20 R. McLaren, S. A. C. Clark, I. Ishii, and A. P. Hitchcock, Phys. Rev. A, **36**, 1683 (1987).

21 S. R. P. Silva, J. Robertson, Rulsli, G. A. J. Amaratunga, and J. Schwan, Phil. Mag. B, **74**, 369 (1996).

22 H. Efstathiadis, Z. Akkerman, and F. W. Smith, J. Appl. Phys, **79**, 2954 (1996).

23 D. R. McKenzie, D. Muller, and B. A. Pailthorpe, Phys. Rev. Lett., **67**, 773 (1991).

24 D. R. McKenzie, J. Vac. Sci. Technol. B, **11**, 1928 (1993).

25 J. Robertson, Diamond Relat. Mater., **3**, 361 (1994).

26 H. Yokomichi, and K. Morigaki, J. Non-Cryst. Solids., **266-269**, 797 (2000).

27 M. Weiler, J. Roberson, S. Sattel, V. S. Veerasamy, K. Jung, and H. Ehrhardt, Diamond Relat. Mater., **4**, 304 (1995).

28 M. Weiler, S. Sattel, T. Giessen, K. Jung, H. Ehrhardt, V. S. Veerasamy and J. Robertson, Phys. Rev. B, **53,** (1996) 1594.

29 R. G. Lacerda, F. C. Marques, and Freire Jr, Diamond Relat. Mater., **8**, 495 (1999).

30 A. Staudinger and S. Nakahara: Thin Solid Films **45** (1977) 125.

31 H. Yokomichi, and K. Morigaki, J. Non-Cryst. Solids., **266-269**, 797 (2000).

32 K. P. Huang, P. Lin, and H. C. Shih, Jpn. J. Appl. Phys. **42**, 3598 (2003).

Chapter 7

Electric Properties

7-1 Introduction

The capacitance and leakage current of a-C:F films can be measured by HP 4280 and HP 4156. We can calculate the dielectric constant and estimate the conductivity of the films. The higher flow ratio a-C:F films have a lower dielectric constant and a low leakage current. The electric properties a-C:F films will change when being annealed at 300℃. The dielectric constant increases at the rise of temperature, while the leakage current declines. The dielectric constant decreases when fluorinated concentration goes up. A low dielectric constant of around 1.5 and high dielectric strength beyond 35 MV/cm were obtained from R = 0.98 a-C:F films in the as-deposited and annealed conditions.

7-2 Experiment

The metal-insulator-metal (MIM) structure (Pt/a-C:F/Pt) was used for electric property measurements (Fig. 7-1). The bottom Pt electrodes were deposited by sputter tool, and the top electrodes were deposited by electron gun (e-gun) tool. Current-voltage (I-V) measurements were performed with the HP4156, and the capacitance (C-V) characteristic was measured with the HP4280 at a frequency of 1MHz. The flowchart of measurement method is shown in Fig. 7-2.

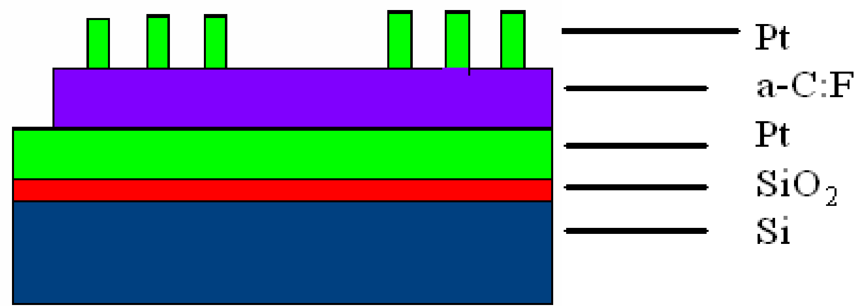

Figure 7-1 shows the schematic structure of MIM (Pt/a-C:F/Pt).

3 Inches N-type Si

RCA Cleaning

Dry Oxide Growth

Sputtering Pt

ECR-CVD
a-C:F

Annealing
300°C

Pt E-gun

HP 4156
I-V

HP 4280
C-V

Figure 7-2 shows the measuring methods of electronic properties.

7-2-1 Deposition of Insulator

We used SiO_2 which was grown on silicon wafer as an insulator layer in this study. The 1500Å thermal oxide was grown at 950℃ in a steam atmosphere (ASM furnace). The metal-insulator-metal structure was used to measure the electronic properties of a-C:F films.

7-2-2 Deposition of Metal Thin Film

The MIM (metal/insulator/metal) structure was used for electronic properties measurement. We sputtered 1000 Å Pt as the bottom electrode, and used E-gun to deposit 600 Å Pt as a top electrode.

7-3 Results and Discussion

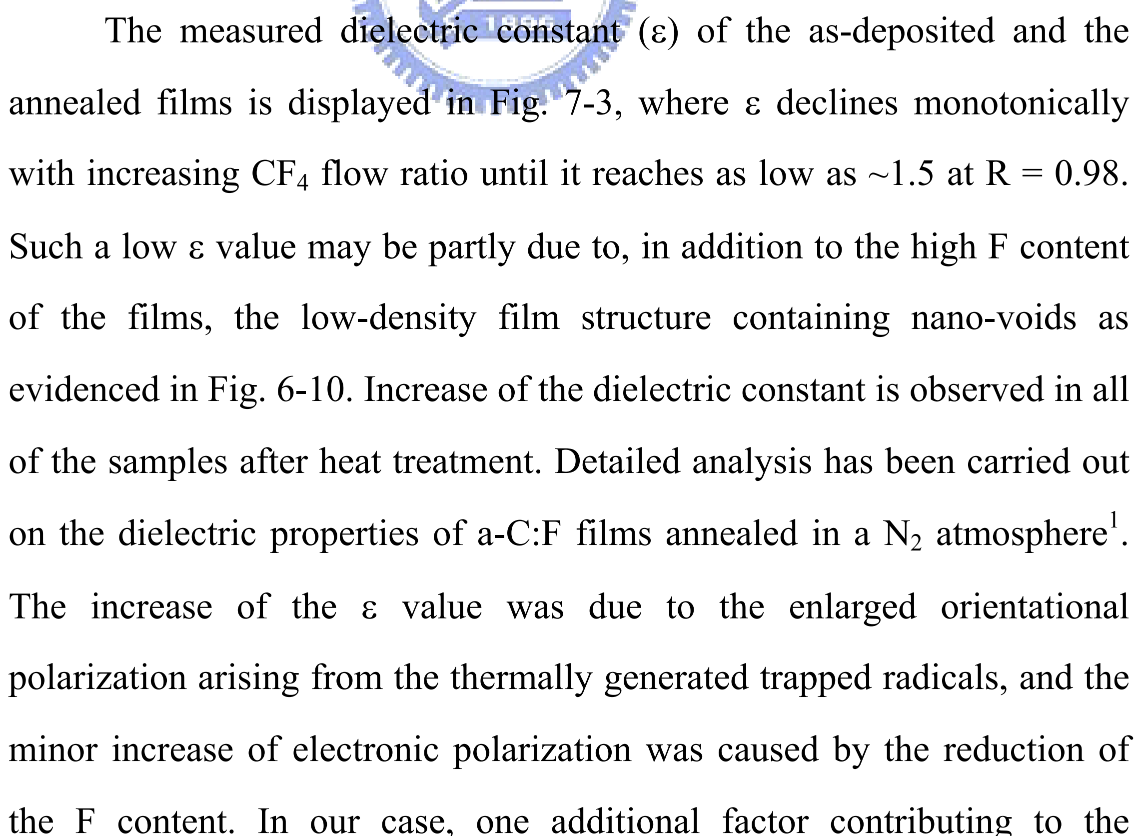

The measured dielectric constant (ε) of the as-deposited and the annealed films is displayed in Fig. 7-3, where ε declines monotonically with increasing CF_4 flow ratio until it reaches as low as ~1.5 at R = 0.98. Such a low ε value may be partly due to, in addition to the high F content of the films, the low-density film structure containing nano-voids as evidenced in Fig. 6-10. Increase of the dielectric constant is observed in all of the samples after heat treatment. Detailed analysis has been carried out on the dielectric properties of a-C:F films annealed in a N_2 atmosphere[1]. The increase of the ε value was due to the enlarged orientational polarization arising from the thermally generated trapped radicals, and the minor increase of electronic polarization was caused by the reduction of the F content. In our case, one additional factor contributing to the

increase of the dielectric constant is probably the shrinkage of voids which enhanced the film density.

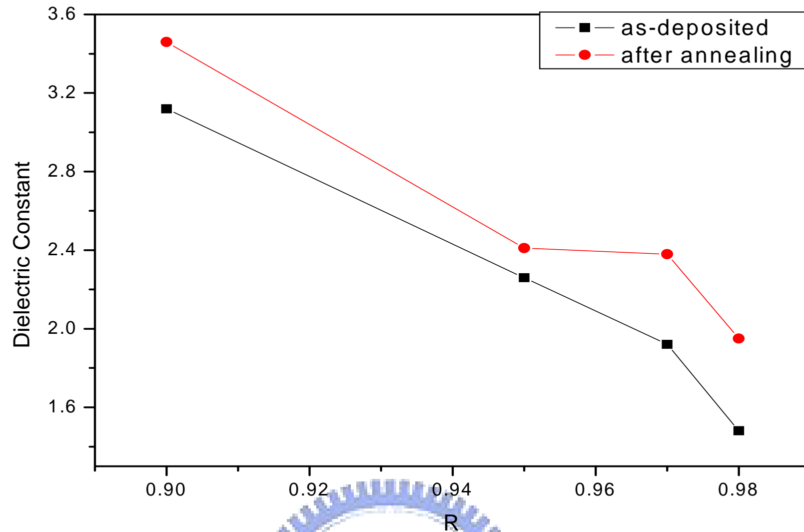

Figure 7-3. Dielectric constant of the films as function of the CF_4 flow ratio R.

Among the measured I-V curves of the as-deposited films, many of them showed either a huge transient current spike or a breakdown at field intensity depending on the samples (Fig. 7-4). The current surges are normally attributed to a low-resistance path formed in the films during discharge[2,3], where the low-resistance path, in the case of the transient spike, would form a open-circuit, then, a self-healing process. In general, microstructure defects presumably work to trigger the discharge and initiate the formation of the low-resistance path. In the current study, an inhomogeneous, high local field intensity, which is capable of triggering

the discharge, may be induced near the irregular morphology of the nano-voids when an external field is applied across the films. The shrinkage of voids after annealing might be responsible for the deletion of breakdowns in the I-V characteristics of the annealed a-C:F films, which demonstrated superior dielectric strength compared with that of SiO_2 films. The annealed sample of R = 0.98 with a thickness of around 400 Å showed a high dielectric strength beyond 35 MV/cm, while for SiO_2 film with the same thickness, the highest field strength it could sustain is around 10 MV/cm[4].

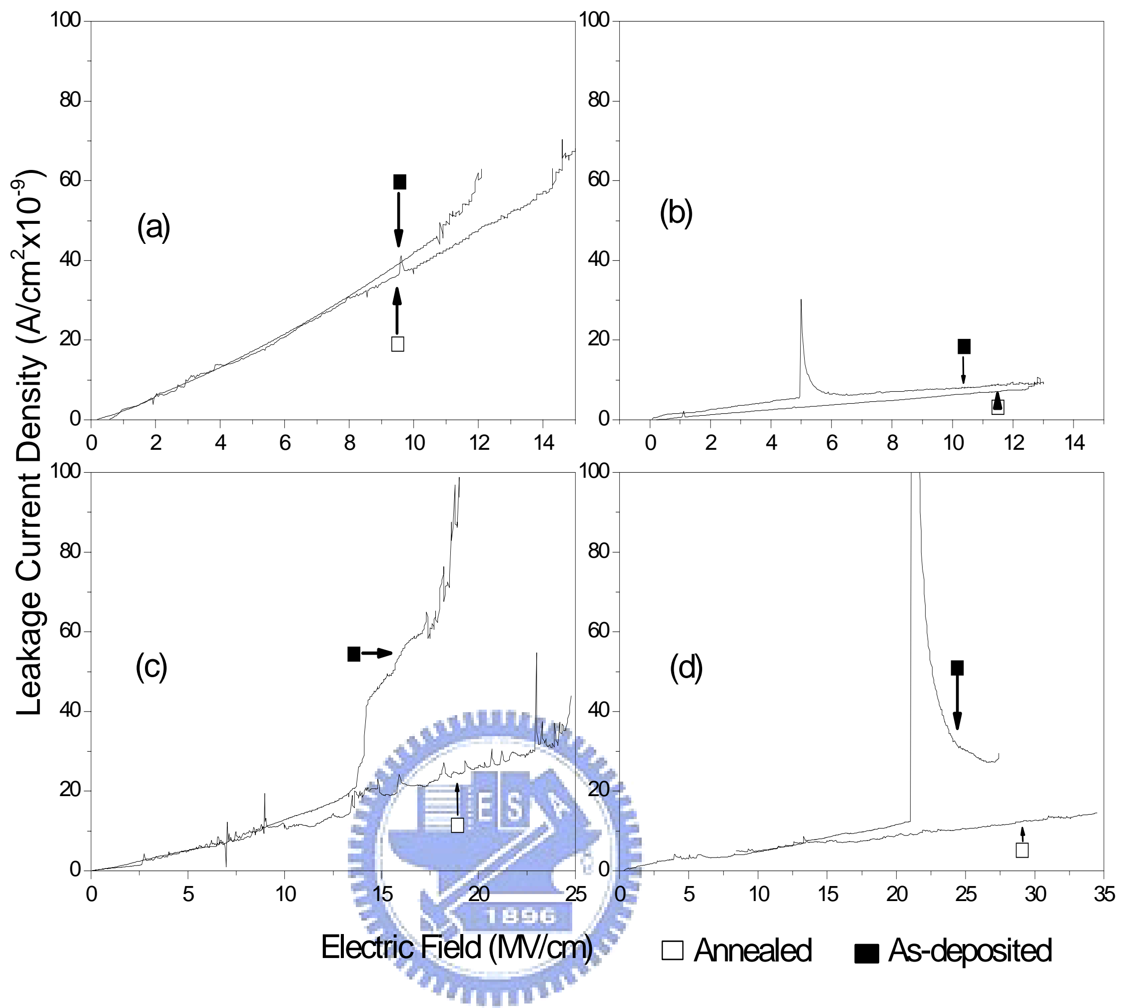

Fig. 7-4. Leakage current of the a-C:F films of (a) R = 0.98, (b) R = 0.97, (c) R = 0.95, (d) R = 0.90.

The magnitude of the current surges decreases when the flow ratio goes down, and eventually diminishes in the sample with R = 0.90. The above variation is consistent with the fact that fewer nano-voids are found in the as-deposited samples at a lower flow ratio. In contrast, the increase of normal leakage current at a decreasing flow ratio was observed in the annealed films (Fig. 7-4), and the variation was expressed in terms of averaged electrical conductivity versus flow ratio as shown in Fig. 7-5. Similar results have been reported in previous studies[5,6], where the higher conductivity of a-C:F films was attributed to their higher sp^2/sp^3 bonding fraction (sbf), considering that the graphitic, sp^2 bonded carbon, is more conductive than the diamond-like, sp^3 bonded carbon. Consistent results for the measured sbf of the annealed films are displayed in Fig. 7-6. It is noted that the conductivity increased slowly with an increasing sbf in the CF_4 flow ratio from R = 0.98 to 0.95. The conductivity then increases rapidly at around sbf = 40%, which indicates a threshold fraction of sp^2 bonded carbons for charge conduction. Further studies are needed to delineate the dependence of charge carrier concentration and mobility on the sp^2/sp^3 bonding fraction.

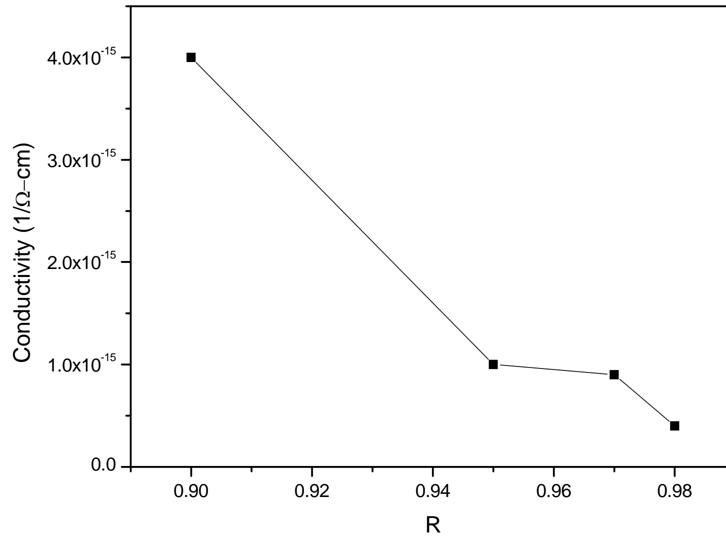

Fig. 7-5. Electrical conductivity of the annealed films as a function of the CF_4 flow ratio R.

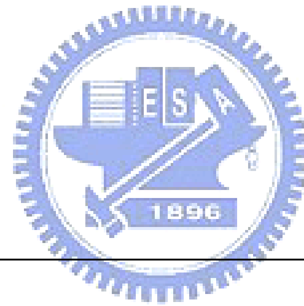

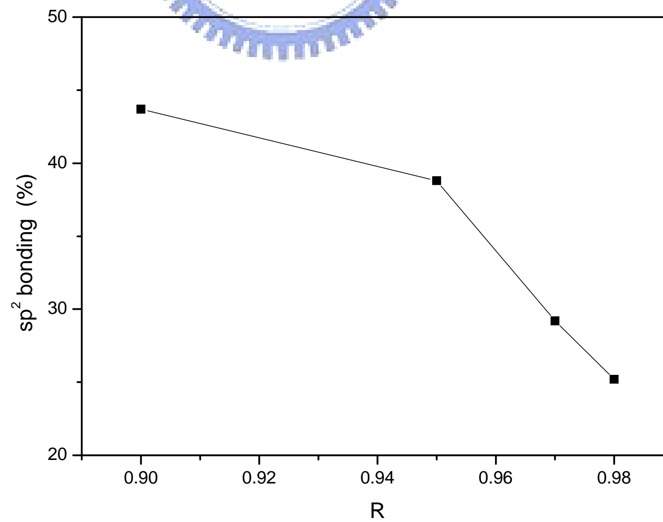

Fig. 7-6. sp^2/sp^3 bonding fraction of the annealed films as a function of the CF_4 flow ratio R.

7-4 Summary

By heat treatment the fluorine concentration will be decreased and the orientational polarization will be enlarged. The dielectric constant of a-C:F films rise at a negative rate in CF_4 flow ratio. The shrinkage of voids after annealing is responsible for the deletion of breakdowns in the I-V characteristics of the annealed a-C:F films. The higher flow ratio in a-C:F films generates more sp^3 structures which lowers the electric conductivity. The dielectric constant of the as-deposited films can be as low as 1.5 for those prepared at a high flow ratio, and the dielectric strength of the annealed films is beyond 30 MV/cm, far superior to that of SiO_2 films with the same thickness. The occurrence of a huge transient current spike or breakdown during the I-V test was attributed to the nano-voids found in the as-deposited films, which worked to trigger the discharge. The averaged conductivity of the films was related to the measured sp^2/sp^3 bonding fraction which indicated a threshold fraction of around 40%.

Reference

1 K. Endo and T. Tatsumi, J. Appl. Phys. **86**, (1999) 2739.

2 N. Klein, Thin Solid Films **7**, (1971) 149.

3 J. C. Jackson, T. Robinson, O. Oralkan, D. J. Dumin and G. A. Brown, J. Electrochem. Soc. **145**, (1998) 1033.

4 P. Solomon, J. Vac. Technol. **14**, (1997) 1122.

5 H. Yang, D. J. Tweet, Y. Ma and T. Nguyen: Appl. Phys. Lett. **73** (1998) 1514.

6 J. P. Chang, H. W. Krautter, W. Zhu, R. L. Opila and C. S. Pai: J. Vac. Sci. & Technol. A. **17** (1999) 2969.

Chapter 8

Optical Properties

8-1 Introduction

Both a-C:F film and a-C:H film consist of carbon sp^3 and sp^2 bonds. Therefore, the optic properties of a-C:F films are similar to that of a-C:H films. The sp^2 content and the fluorine concentration would affect the photoluminescence lifetime, as well as energy band gap of the a-C:F films. A lifetime of around 0.34 μsec and an energy gap of ~ 2.75 eV were observed in both the as-deposited and after annealing conditions. The higher sp^3 content and the fluorine concentration make the PL peak site of a-C:F film blue-shift, and make energy band gap become higher. The short carrier lifetime in the a-C:F film makes the PL peak blue-shift. The annealing changed both the structure and composition of the a-C:F film. The type of fluorocarbon bonds and electronic structure characterized the mechanical and physical properties of a-C:F film.

8-2 Experiment

In order to get stronger spectra signal of the a-C:F films, the thickness of a-C:F films was deposited 1 μm on silicon wafers in ECR-CVD which is for PL, pulse laser and n&k measurements. We also deposited 1 μm a-C:F films on 7059 glasses in ECR-CVD for UV/VI measurement. The fluorescence was measured by the PL apparatus using a helium-cadmium (He-Cd) laser (λ= 325 nm) as the excitation source. An

Excimer pulse laser (λ=193 nm) was used to evaluate photoluminescence lifetime. The UV/VI and n&k spectrometers were used to measure the optical band gap of a-C:F films. The experiment flowchart was shown in Fig. 8-1.

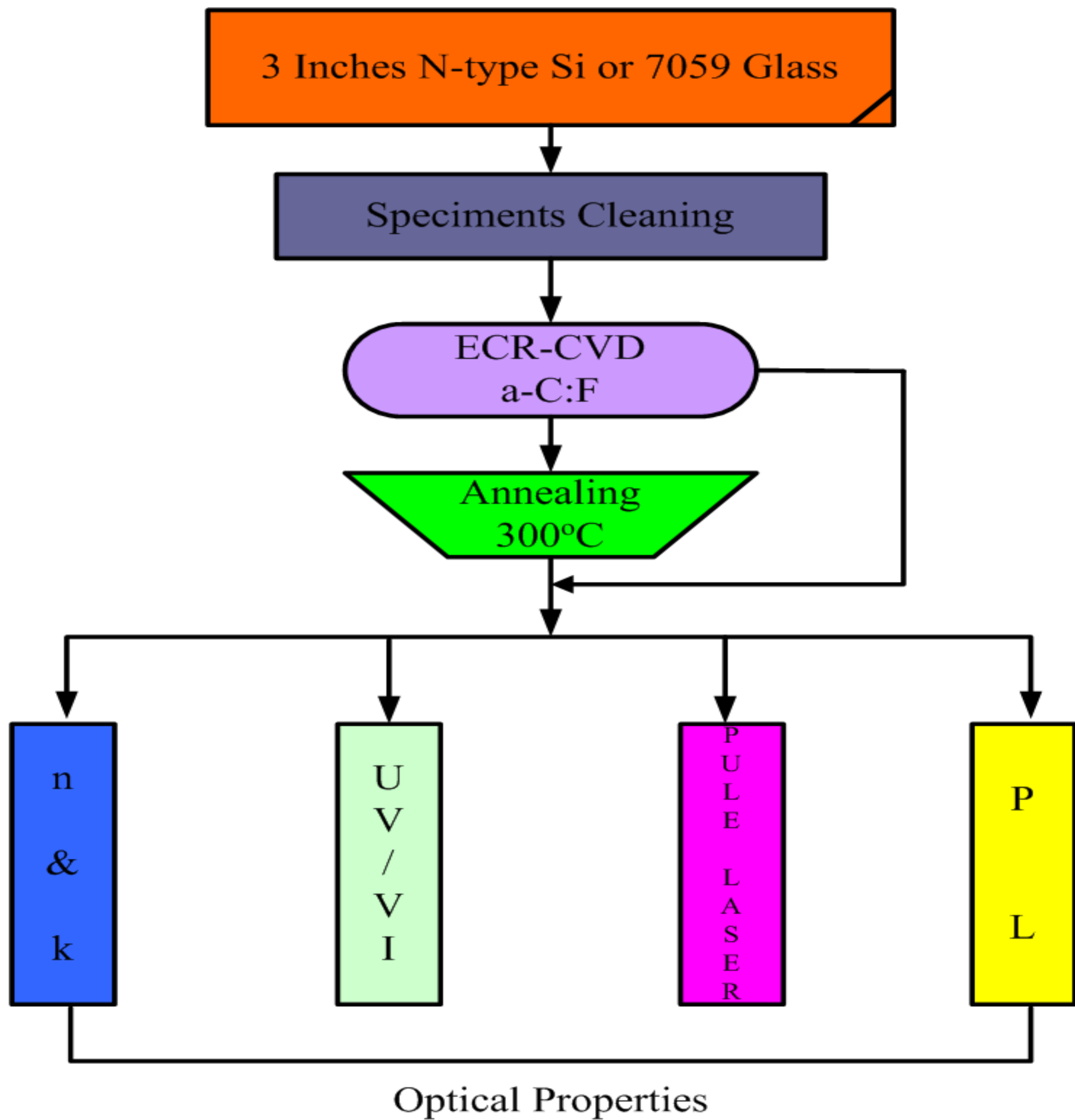

Figure 8-1 The experiment flowchart for optical measurement.

8-3 Results and Discussion

The a-C:F film has a broad band luminescence characteristic of an amorphous semiconductor with broad band tails. Figure 8-2 shows PL spectra for R = 0.97 and R = 0.90 a-C:F films in both as-deposited and after annealing conditions. The PL peak band is like rough Gaussian Peak, and changes with the CF_4 flow ratio. The PL peak site tends to be blue-shifted as the fluorine concentration increases. It is also noticed that annealing helps to reduce the FWHM of the PL spectra. The broad spectrum results from structural disorder of the a-C:F film. Fluorinated amorphous carbon films after the annealing treatment will be structurally relaxed because the disappearance of electron-hole pairs reduces the probability of the radiative recombination[1]. The higher fluorine concentration, which generates more sp^3 in the film, makes the as-deposited a-C:F films blue-shift at high flow ratio.

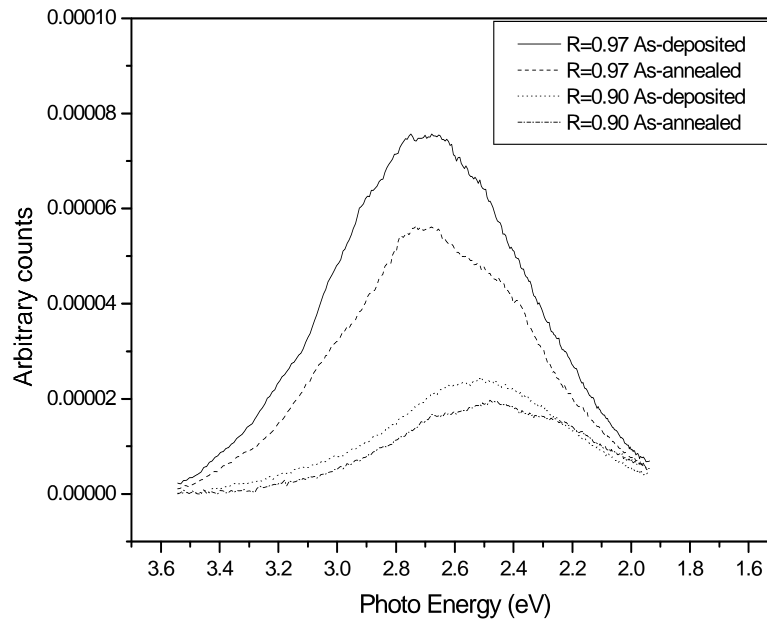

Fig. 8-2. PL spectra produced at R=0.97 and at R=0.90 of a-C:F films for both as-deposited and after annealing.

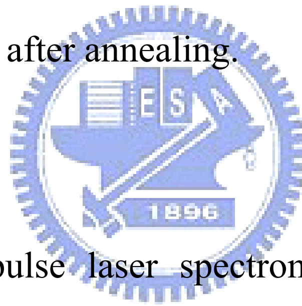

The excimer pulse laser spectrometer was used to measure the lifetime (τ) of the photoluminescence. The results are shown in Fig. 8-3. The lifetime is directly proportional to both fluorine concentration and sp^2 % for both as-deposited and after annealing films. The lifetime is longer in a-C:F(10^{-7} s) film than in a-C:H(10^{-8} s)[2,3] one, but is much shorter than in a-Si:H(10^{-3} s)[4,5] one. The short lifetime carriers reduce their energy relaxation into lower energy states and then increase the average energy of carriers in the band tail state[6]. The short photoluminescence lifetime causes a blue-shift of the lowest energy accessible to carriers for radiative recombination in the band tail state[7]. Therefore, we can observe the pronounced blue-shift of the PL peak in a-C:F film, because of the short carrier lifetime.

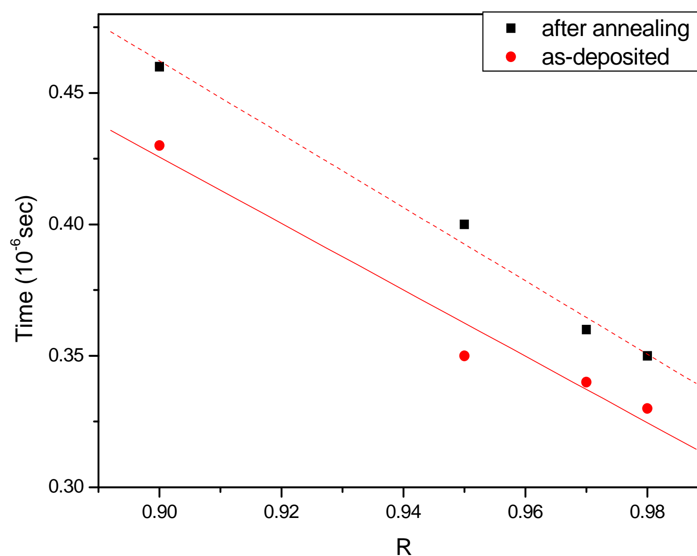

Fig. 8-3 illustrates the photoluminescence lifetime of as-deposited and after annealing a-C:F films.

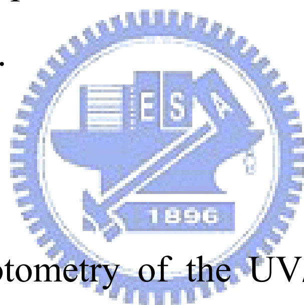

The spectrophotometry of the UV/VI bands of the a-C:F films is plotted in Fig. 8-4. The optical band gap showed in Fig. 8-5 was determined by the Tauc mode[8]. Since the C-F bond energy (102 kcal/mole) is higher than the C-C bond energy (80 kcal/mole), the greater number of fluorocarbon bonds in the a-C:F film produced at higher CF_4 flow ratios will give rise to a higher optical band gap. In addition, the C=C bonds or graphite-like sp^2 structures will lower the optical band gap[9], so the optical band gap of the as-deposited a-C:F film is larger than the one after annealing. This is also the reason why the R = 0.97 film has less blue-shift than the R = 0.90 film. The optical properties are closely correlated to the amount of fluorine incorporated into the films. The increase in the optical band gap energy indicates that the fluorine incorporated into the a-C:F film

has modified the chemical structure of the film towards the higher sp^3 bonding fraction[9]. These properties are similar to those of hydrogenated amorphous carbon[10-12].

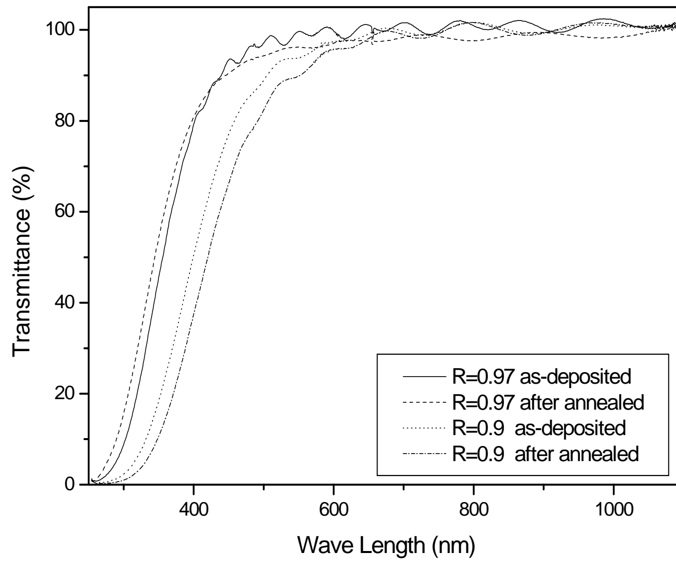

Fig. 8-4. UV/VI spectra of both R=0.97 and 0.90 of the a-C:F films as-deposited and after-annealed at 300°C.

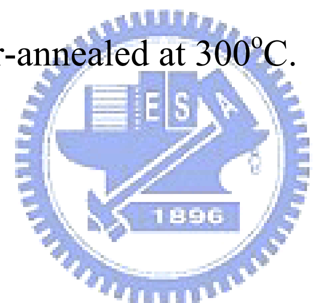

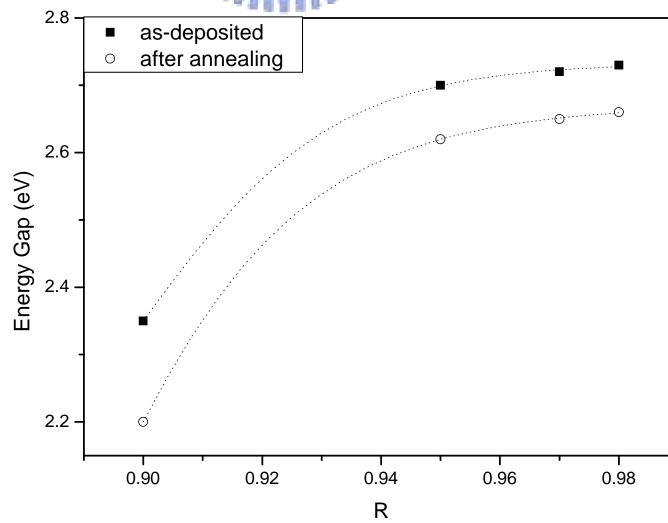

Fig. 8-5 shows the energy gap of as-deposited and 300℃ annealing a-C:F films.

8-4 Summary

The high fluorine concentration of a-C:F films makes PL peak blue-shift, and it has short lifetime carriers. In addition, the higher fluorine concentration of a-C:F films generates more C-F bonds in the films, and is helpful to form higher energy band gap in the a-C:F films. The higher fluorine concentration will promote a greater number of fluorine carbon bonds in the film and therefore produce a higher optical band gap. Furthermore, annealing will induce the sp^2 structure in the a-C:F film, which will extend the photoluminescence lifetime. The short carriers lifetime in the a-C:F film makes PL peak blue-shift, which is similar to a-Si:H films.

Reference

1 S. R. P. Silva, J. Robertson, Rulsli, G. A. J. Amaratunga, and J. Schwan, Phil. Mag. B, 74 (1996) 369.

2 Rusli, Gehan A. J. Amaratunga, and J. Roberson, Phys. Rev. B, 53 (1996) 16306.

3 W. Lormes, M. Hundhausen, and L. Ley, J. Non-Cryst. Sol. 227-230 (1998) 570.

4 W. Siebert, R. Carius, W. Fuhs, and K. Jahn, Phys. Stat. Sol. B, 140 (1987) 311.

5 S. Liedtke, K. Lips, M. Bort, K. Jahn, and W. Fuhs, J. Non-Cryst. Sol., 114 (1989) 522.

6 Y. Kanemitsu, M. Liboshi, and T. Kushida, Appl. Phys. Lett., **76**, 2200

(2000).

7 M. J. Estes, and G. Moddel, Appl. Phys. Lett., **68**, 1814 (1996).

8 Richard Zallen, The Physics of Amorphous Solids (Second Edition), Wiley, New York, 1998.

9 A. Weber, R. Pöckelmann, and C.-P. Klages, J. Vac. Sci. Technol. A. **16**, 2120 (1998).

10 M. Weiler, S. Sattel, T. Giessen, K. Jung, H. Ehrhardt, V. S. Veerasamy and J. Robertson, Phys. Rev. B, 53 (1996) 1594.

11 Th. Frauenheim, G. Jungnickel, U. Stephan, P. Blaudeck, S. Deutschmann, M. Weriler, S. Sattel, K. Jung, and H. Ehrhardt, Phys. Rev. B, 50 (1994) 7940.

12 M. Hakovirta, X. M. He and M. Nastasi, J. Appl. Phys., **88**, 1456 (2000).

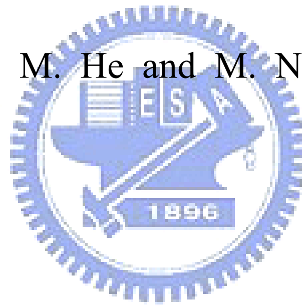

Chapter 9

Conclusions, and Suggestions for Future Study

9-1 Conclusion

a-C:F films of high fluorine content were obtained by ECR-CVD method using tetrafluoromethane (CF_4) and acetylane (C_2H_2) as precursor gases. Dielectric constant of the as-deposited films can be as low as 1.5 for those prepared at a high CF_4 flow ratio, and dielectric strength of the annealed films is beyond 30 MV/cm, far superior to that of SiO_2 films with the same thickness. The huge transient current spike or a breakdown occurring during the I-V test was attributed to the nano-voids found in the as-deposited films which work to trigger the discharge. The averaged conductivity of the films was related with the measured sp^2/sp^3 bonding fraction which indicated a threshold fraction at around 40%.

The sp^3 bond ratio can be increased by the fluorine concentration through an increase in the fluorocarbon flow ratio. The FTIR and ESCA results reveal that the structure of the a-C:F films prepared at various CF_4 flow ratios are different. Furthermore, the result of HREELS reveals that annealing of the films increases the carbon double bond structures in the a-C:F films. The higher CF_4 flow ratios, not only produce more sp^3 linear structures, but also smooth and soften the a-C:F films. There is a lot of structural variation after annealing; therefore, the electrical and optical properties of the a-C:F films are different from these of the as-deposited films. The higher fluorine concentration promotes a greater number of

fluorine carbon bonds in the films and therefore produces a higher optical band gap. Furthermore, annealing induces the sp^2 structure in the a-C:F film, which will extend the photoluminescence lifetime. The short carriers lifetime in the a-C:F film makes PL peak blue-shift.

9-2 Suggestions for Future Study

There are a number of studies needed to be done in the future. There are physical and chemical properties to be investigated. The following topics are suggested for the future studies:

(1) Improving the hardness of a-C:F films.

(2) Delineating the dependence of charge carrier concentration and mobility on the sp^2/sp^3 bonding fraction.

(3) Increasing the thermal stability of a-C:F films.

(4) Investigating the field emission properties.

(5) Developing a novel characterization metrology to measure the porosity of low k films.

簡歷

姓名: 黃昆平

性別: 男

年齡: 33 歲 (民國 60 年 7 月 30 日生)

籍貫: 台灣省苗栗縣

地址: 苗栗縣南庄鄉員林村 5 鄰小南埔 41 號

學歷: 國立台北工業專科學校礦冶工程科材料組畢業

(76 年 9 月- 81 年 6 月)

國立中興大學材料工程科畢業

(84 年 9 月- 86 年 6 月)

國立交通大學材料科學與工程學系畢業

(86 年 9 月- 93 年 6 月)

博士論文題目:

氟化非晶質碳膜之性質

The Properties of Fluorinated Amorphous Carbon Films

經歷：1. 中華民國斐陶斐(Phi Tau Phi)榮譽學會會員(86 年 6 月)。

2. 91 年 9 月至 92 年 8 月至德國 Max-Planck Institute (MPI) Stuttgart 固態物理研究所當交換學生一年。期間參與 MPI 及 Infineon 公司共同合作“單壁及多壁奈米碳管在不同電極上

的電子傳輸”之研究。

Publications

Journal Papers:

1. K. P. Huang, and H. C. Shih, " Preparation of high hard DLC Films by ECR-CVD. Master Thesis.
2. S. L. Sung, X. J. Guo, K. P. Huang, F. R. Chen and H. C. Shih, "The strengthening mechanism of DLC film on silicon by MPECVD", Thin Solid Film, 340 (1998) 169.
3. S. L. Sung, T. G. Tsai, K. P. Huang, J. H. Huang and H. C. Shih, "The Effect of D. C. Bias on the Synthesis of Crystalline Carbon Nitrides on Silicon by Microwave Plasma Enchanced Chemical Vapor Deposition (CVD)", Jpn. J. Appl. Phys., 37 (1998) L148.
4. K. P. Huang, P. Lin, and H. C. Shih, "Structure and Electrical Studies of Fluorinated amorphous Carbon Films Prepared by Electron Cyclotron Resorance/Chemical-Vapor Deposition", Jpn. J. Appl. Phys. 42 (2003) 3598.
5. S. H. Lai, K. P. Huang, Y. M. Pan, Y. L. Chen, L. H. Chan, and H. C. Shih, "Electron Field Emission from Fluorinated amorphous Nanoparticles on Porous Alumina" Chem. Phys. Lett. 382 (2003) 567.
6. K. P. Huang, P. Lin, and H. C. Shih, "Structures and Properties of

Fluorinated amorphous Carbon Films”, J. Appl. Phys. **96**, 354 (2004).

Conference:

1. H. C. Shih, S. L. Sung, T. G. Tsai and K. P. Huang, 1997, "Synthesis and Characterization of Carbon Nitride Film on Silicon by Microwave Plasma Enhanced CVD", International Symposium on Surfaces and Thin Films, Academia Sinica and SRRC, Taipei, Taiwan, March 25-28.
2. H. C. Shih, S. L. Sung, F. R. Chen, X. J. Guo and K. P. Huang, 1997, "The Strengthening Effect of DLC Coating on Silicon prepared by MPECVD", International Conference on Metallurgical Coatings and Thin Films, Abstract DP17, San Diego, CA., April 21-25.
3. X. J. Guo, S. L. Sung, K. P. Huang and H. C. Shih, 1997, "Effects of D.C. Bias Voltage on the Formation of Interfacial Layer of Diamond on Silicon by MPECVD Synthesis", 8th European Conference on Diamond, Diamond-like and Related Materials jointly with Applied Diamond Conference 1997 and 4th International Conference on the Applications of Diamond Films and Related Materials, Abstract 15.004, Heriot-Watt University, Edinburgh, Scotland, 3-8 August
4. X. W. Liu, K. P. Huang, J. H. Lin, L. T. Chao, P. Lin, and H. C. Shih,

"Deposition of Thermal Stable Amorphous Carbon Nitride Thin Films with Low Dielectric Constants by ECR-CVD", American Vacuum Society 47th International Symposium, Boston USA, October 2-6 (2000).

5. H. C. Shih, S. L. Sung, T. G. Tsai and K. P. Huang, 1997, "Synthesis and Characterization of Carbon Nitride Film on Silicon by Microwave Plasma Enhanced CVD", International Syposium on Surfaces and Thin Films, Academia Sinica and SRRC, Taipei, Taiwan, March 25-28.
6. Y. L. Chen, K. P. Huang, Shih-Hsiang Lai , Yi-Min Pan, P. Lin, H. C. Shih, "Synthesized The Low Dielectric Constant Material of Fluorinated Amorphous Carbon Films by ECR-CVD ", Proceeding of The 2002 Annual Conference of The Chinese Society of Materials Science , November 22-23 (2002) 72, Taipei.
7. Yi-Min Pan, Shih-Hsiang Lai , Y. L. Chen, K. P. Huang, P. Lin, H. C. Shih, "Preparing and Analyzing Doped Nitrogen Fluorinated Amorphous Carbon by ECR-CVD, and Characterized, November 22-23(2002) 74, Taipei.
8. K. P. Huang, Pang Lin, S. Roth, The Electronic Properties of Fluorinated Amorphous Carbon, Proceeding of Science and Technology of Organic

Semiconductors, 09-11 December 2002 at Physikzentrum Bad Honnef (Germany).